Analysis of Hydrogen Pumping on Stirred Tank Reactor Polymer Electrolyte Membrane Fuel Cell for Hydrogen Purification

Hannah F. Xu, ChE'08

Spring 2008

Thesis Advisor: Prof. J. Benziger

Submitted in partial fulfillment of the requirements for
the degree of Bachelor of Science in Engineering

Department of Chemical Engineering
Princeton University

This paper represents my own work in accordance with University regulations.

I authorize Princeton University to lend this thesis to other institutions or individuals for the purpose of scholarly research.

Hannah Xu

I further authorize Princeton University to reproduce this thesis by photocopying or by other means, in total or in part, at the request of other institutions or individuals for the purpose of scholarly research.

Hannah Xu

To my parents for loving, encouraging, and trying to understand what I am doing.

To my dog, Happy, who is the world’s perfect energy source to deliver joy to anyone and everything.

To my friends who have laughed, suffered, and put up with me through rain and shine.

Acknowledgements

I am indebted to Prof. Benziger for giving me the opportunity to work in his lab, for his never-ending insight into science, for his patience and guidance, and most importantly, for showing me what the lethal combination of curiosity, dedication, and humility can accomplish.

I like to thank graduate students, Erin Kimball and May Jean Cheah, for helping me launch and direct my thesis work, letting me use already-cleaned Nafion 115, as well as for the countless troubleshooting and advice I received along the way.

I am grateful for Barry and Larry's work in the SEAS machine shop to transform my fuel cell sketch into my heart and soul during the spring of my senior year.

Abstract

A stirred tank reactor (STR) polymer electrolyte membrane fuel cell (PEMFC) was built and analyzed as a hydrogen pump. By applying an outside current, the fuel cell pumps hydrogen from the anode to the cathode. Dynamics of the fuel cell were analyzed at different gas inlet compositions, inlet flow rates, temperatures, external load resistances, and applied currents to explore hydrogen pumping as an alternative method to hydrogen purification.

Once the internal resistance of the STR PEM fuel cell was verified to correspond with literature, the fuel cell underwent manual- and Arbin- regulated hydrogen pumping operations. Humidity tests showed a decrease in relative humidity of the inlet feed streams at high fuel cell temperatures. This meant that the MEA was prone to drying out at higher fuel cell temperatures. However, higher fuel cell temperatures were also found to enable H_2 to more competitively adsorb onto Pt catalysts in the presence of CO_2. High-slope voltage regions detected in current sweeps were investigated.

Table of Contents

List of Figures

1. Introduction

a. Fuel Cell Vehicles (FCVs)

Some scientists and economists predict that automobiles of the future, in the form of fuel cell vehicles (FCVs), will have market viability in the next twenty years [23]. President Bush's Freedom Car program is an example of the dozens of governmental funding and programming aimed to bring FCV costs comparable to that of conventional internal combustion and diesel engines. With increasing government and civilian interests in finding clean alternative energy to alleviate fossil fuel shortages and global warming, more research has turned to advancing hydrogen/ oxygen proton electrolyte membrane (PEM) fuel cells. PEM fuel cells are attractive for its low temperature operations, fast response to load changes, long life, low to zero emissions of environmental pollutants (CO, NO, VOCs, and SO_x), good water retention, high specific conductivity within the fuel cell membrane, and higher theoretical efficiencies for energy conversion [8, 16, 17]. Most PEM fuel cells operate under excess hydrogen fuel to undergo an electrochemical reaction with oxygen to generate electric power. They also require pure hydrogen inlet streams with less than 20ppm CO concentrations to avoid poisoning of the catalyst [21]. Therefore, hydrogen purification, a currently inefficient and expensive operation, is an immediate concern for the viability of FCVs.

b. Senior Thesis Topic

This study involved building and testing a stirred tank reactor (STR) PEM fuel cell system to run as a hydrogen pump to carry out hydrogen purification. Hydrogen pumping contrasts from standard hydrogen fuel cell operations, in that when hydrogen is fed into the anode, hydrogen, rather than water is produced at the cathode. The hydrogen pump necessitates an external current to drive hydrogen from the anode to the cathode. The separation of H_2 from an anode inlet stream of H_2 with N_2 or CO_2 was analyzed as functions of temperature, gas composition, flow rate, current, and external load resistance. The study employed Nafion, a Teflon/ perfluorosulfonic acid co-polymer as the polymer electrolyte in the membrane, electrodes of Pt catalyst on carbon cloth, and gas streams H_2, O_2, N_2, and CO_2.

2. Background

a. Hydrogen Production

Hydrogen, the fuel for FCVs, is produced in bulk predominantly from fossil fuels. Hydrocarbon fossil fuels such as natural gas produce hydrogen with approximately 80% efficiency [15]. The process involves steam reforming followed by water gas shift reactions, and releases greenhouse gases. Steam (H_2O) and methane (CH_4) undergo an endothermic reaction at 700-1100^oC to yield hydrogen (H_2) and carbon monoxide (CO). Hydrogen production continues when the carbon monoxide of the steam reforming product stream undergoes an exothermic reaction at 130^oC to yield carbon dioxide (CO_2) and hydrogen.

Steam Reforming

$C_nH_{2n+2} + nH_2O \rightarrow nCO + (4n+2)H_2$

Water Gas Shift

$H_2O+CO \leftrightarrow H_2+CO_2$

Coal is another fossil fuel used for hydrogen production. Under high temperatures and pressures, and mixed with steam and oxygen, coal undergoes gasification to break down into CO and H_2.

b. Hydrogen Purification

Hydrogen produced from steam reforming and water gas shift reactions needs to be purified before it is fed into PEM fuel cells. Steam reforming and water gas shift reactions leave CO in the hydrogen product gas stream at 50-100ppm [8]. At this level, CO poisons the Pt catalysts of the fuel cell when the fuel cell temperature is below 100°C. Since FCVs are intended for operation below 100°C, the desired CO level should be less than 20ppm [21].

PEM fuel cell membranes' low CO tolerance can be addressed in different ways: replacing Pt with more CO-tolerant catalysts, or changing the operating environment of the fuel cell [9]. Current research involving Pt-Mo and Pt-Ru catalysts have increased CO tolerance to 50ppm at the expense of increasing Pt loading 5-10 times more than the traditional Pt catalyst [9]. Prof. Benziger's lab is approaching the CO tolerance problem by considering PEM fuel cell operations at 130°C, the temperature in which the desired H_2 adsorption on Pt catalyst becomes competitive with CO adsorption.

Although analysis of PEM fuel cells via different catalysts and operating conditions to solve the CO tolerance problem is important, further research is inapplicable if there is no hydrogen economy to supply hydrogen fuel. The hydrogen economy exists in theory since there is currently no infrastructure or appropriate technology to provide more efficient and less costly hydrogen purification for the market. Current hydrogen purification methods involve membrane separation techniques (palladium, getter, and catalytic membranes), pressure swing adsorption (PSA), and cryogenic distillation.

Membrane separation techniques utilize membranes' physical nature to allow selected materials to pass through. Palladium membranes allow the diffusion of hydrogen under pressure at 300°C to provide less than 1ppb impurity level in the hydrogen product stream. Although this method satisfies the CO tolerance of PEM fuel cell membranes, its 1000 fold decrease in impurity level is unnecessarily costly for FCVs [1]. The getter method absorbs and diffuses impurities irreversibly into its membrane at room temperature. The irreversible reaction implies the need to invest in new getters, which might not prove cost effective in the long run. Lastly, the catalytic membrane method is currently more suitable for the removal of O_2, H_2O, and CO_2 [1]. Membrane separation techniques have attracted the widest interest but still need perfection.

The more extensively used industrial processes for hydrogen purification are PSA and cryogenic distillation. PSA relies on increasing gas partial pressures to adsorb more impurities on adsorbents, yielding products of high-purity of ~99.99% H_2 [1]. Cryogenic distillation is a low-temperature fluid mixture separation process employing differences in boiling temperatures to yield products of moderate-purity of up to 95% H_2 [1]. Both methods are energy intensive and impractical for scales of production.

Prof. Benziger's lab is considering a hydrogen purification approach that pumps hydrogen from the anode to the cathode using a Nafion-based PEM fuel cell. The fuel cell serves as a hydrogen pump via an external power supply that varies its own voltage and resistance to pump H_2 from the anode to the cathode.

c. STR PEM Fuel Cell

Profs. Andy Bocarsly of Chemistry and Jay Benziger of Chemical Engineering at Princeton University have patented stirred tank reactor (STR) polymer electrolyte membrane (PEM) fuel cells operating at ~130^{o}C for potential applications in transportation. Operations at high temperatures serve to discourage the reverse conversion of the water gas shift reaction that results in approximately 100ppm CO in the hydrogen product stream, an impurity level intolerable for FCVs. By running these PEM fuel cells as hydrogen pumps, an alternative to hydrogen purification might be addressed.

i. Standard and Hydrogen Pumping Operations

An explanation of a fuel cell under standard operation is helpful to further the discussion of hydrogen pumping. A PEM fuel cell derives its name from the polymer electrolyte membrane (PEM) sandwiched between its anode and cathode electrodes. A standard hydrogen PEM fuel cell operation involves feeding hydrogen into the anode inlet and oxygen into the cathode inlet (Figure 1a). Hydrogen and oxygen adsorb onto the anode and cathode surfaces, respectively. Once adsorbed, hydrogen is catalytically oxidized into protons and electrons. Voltage, which indicates the chemical potential between the electrodes due to the catalytic oxidization of hydrogen at the electrode/electrolyte surface, is internal for the fuel cell. Only protons travel through the membrane from the anode to the cathode; electrons travel through an external circuit to the cathode. At the cathode, oxygen combines with the crossover protons and electrons; the overall reaction yields water (Equation 1).

$$H_2\,(g) + \tfrac{1}{2}O_2\,(g) \rightarrow H_2O\,(g) \qquad \Delta G^o = -237\text{kJ/mol} \qquad (1)$$

In contrast, when a PEM fuel cell is operated as a hydrogen pump, hydrogen, rather than water, is produced at the cathode outlet (Figure 1b). When molecular hydrogen at the anode is oxidized to protons and electrons at the three-phase interface of catalyst, electroyte, and gas, an applied potential difference pumps protons through the membrane. Voltage is therefore external for the hydrogen pump. Electrons travel through an external circuit to combine with protons to reform molecular hydrogen at the cathode. Figure 1 shows the half reactions at the anode and cathode for each type of operation. The same anodic half reaction occurs for both operations, however, the anode inlet feed for a hydrogen pump usually contains impurities to be separated.

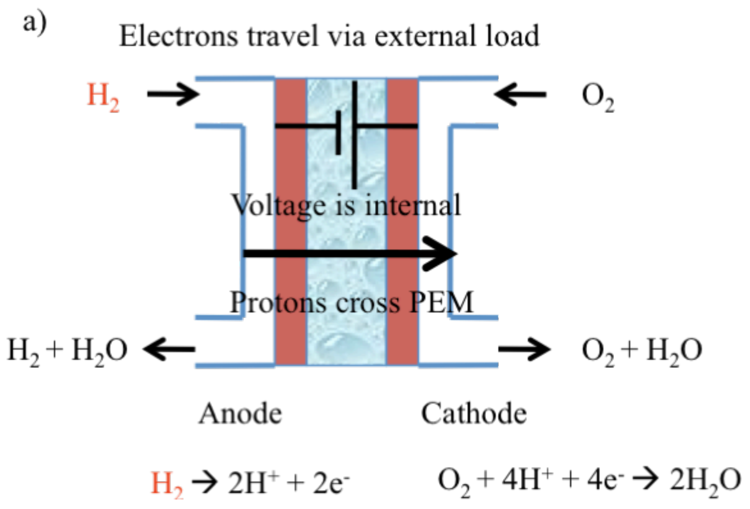

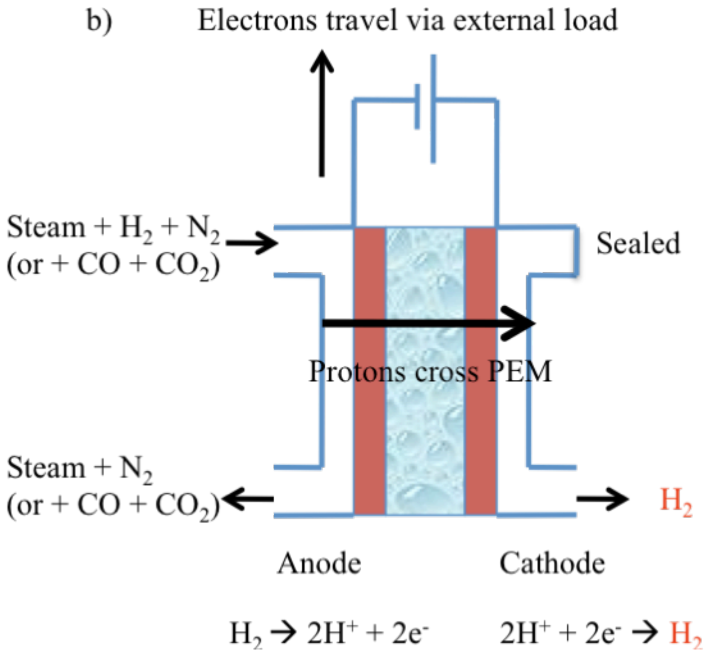

Figure 1. Diagrams of a PEM fuel cell under standard and hydrogen pumping operations with anode and cathode half reactions shown. H_2 is colored red for clarity. a) The diagram of the standard fuel cell operation indicates H_2 as the reactant entering the anode inlet. Voltage is internal for the fuel cell. b) The diagram of hydrogen pumping indicates H_2 as the product exiting the cathode outlet. Voltage is external for the hydrogen pump.

Inlet flow channels at the electrodes are replaced with open gas plenums to yield volume (V_g~$0.2cm^3$). V_g and reactant flow rates (Q) yield a residence time of gases in the plenums, $\tau_R=V_g/Q$, that is equal or greater than the gas phase diffusion time in the plenums $\tau_D=V_g^{2/3}/D_g$ [9]. At this condition, diffusive mixing dominates convective flow to ensure compositional uniformity such that the PEM fuel cell is regarded as a stirred tank reactor (STR). The PEM fuel cell used in this study is assumed to operate at $\tau_R/\tau_D >1$ since the majority of its inlet flow rates falls between 1-20mL/min. For hydrogen pumping with inlet flow rates ~75mL/min (which results in $\tau_R/\tau_D <1$), the STR condition is still assumed to apply. The relaxation of the STR condition is not problematic because the focus on collecting a purified hydrogen outlet stream rather than on the specific dynamics of the fuel cell make the preservation of the STR condition less crucial, the inlet gases can be assumed to be well-mixed in the plenums at the higher flow rates, and a greater hydrogen gradient allows for larger reduction of hydrogen partial pressures to facilitate hydrogen pumping from anode to cathode.

ii. Performance Parameters

Hydrogen and oxygen serve as fuel and oxidant for the fuel cell, respectively. Like batteries, fuel cells generate electricity from chemical reactions. To undergo the overall reaction (Equation 1), a series of processes take place: diffusion of reactants to the electrodes, proton diffusion across the PEM, and heat and water generation and removal. The processes affect fuel cell performance.

The independent system variables of the fuel cell, which include flow rates, composition, heat input, and external load resistance, affect the dependent system variables, which include current, voltage, and membrane water content. Figure 2a, reproduced from Benziger [11], is a fuel cell schematic with independent variables outside and dependent variables inside the dashed box. Resistances of the membrane (R_{int}) and external load (R_L) affect the flow of protons and electrons, which in turn affects the current. A fuel cell circuitry accompanies the schematic (Figure 2b).

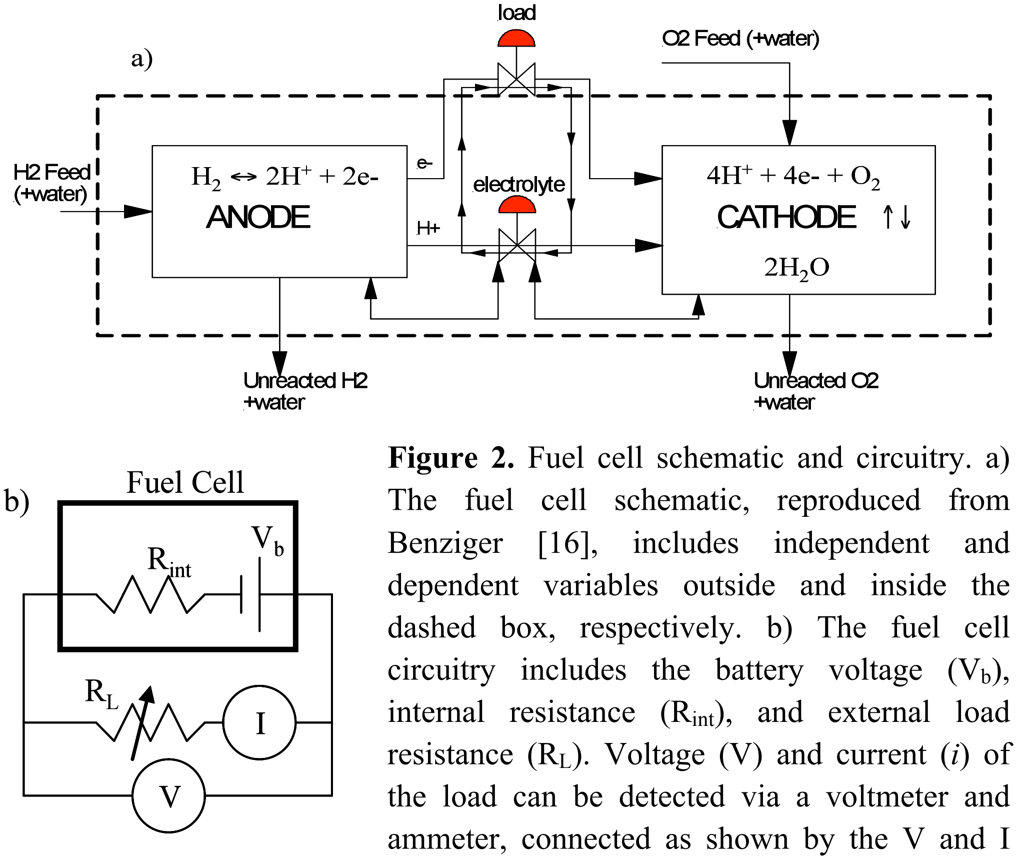

Figure 2. Fuel cell schematic and circuitry. a) The fuel cell schematic, reproduced from Benziger [16], includes independent and dependent variables outside and inside the dashed box, respectively. b) The fuel cell circuitry includes the battery voltage (V_b), internal resistance (R_{int}), and external load resistance (R_L). Voltage (V) and current (*i*) of the load can be detected via a voltmeter and ammeter, connected as shown by the V and I circles, respectively.

The battery voltage, V_b, indicates the chemical potential between the electrodes due to the catalytic oxidization of hydrogen at the electrode/electrolyte surface. Equation 2 shows that V_b is dependent on the membrane water activity via $P_w^{cathode}$. At the anode, the hydrogen activity is determined by the interaction of the partial pressure of hydrogen in the anode inlet, the diffusion through the gas diffusion layer, and the rate of hydrogen consumption in the fuel cell reaction. At the cathode, the hydrogen activity is determined by the equilibrium of oxygen and water. k_A and k_C are mass transfer coefficients determined by electrode porosity, pore tortuosity, electrode thickness, and gas diffusivity.

$$V_b = -\frac{\Delta G^o}{4\text{F}} + \frac{RT}{4\text{F}}\ln\frac{\left(P_H^{anode} - {}^{i}\!/_{2\text{F}k_A}\right)^2\left(P_O^{cathode} - {}^{i}\!/_{2\text{F}k_C}\right)}{\left({}^{P_w^{cathode}}\!/_{P_w^o}\right)^2 P_{total}} \qquad (2)$$

V_b drives a current across two resistances: R_{int}, which makes up the bulk of the membrane resistance (R_m), and R_L, the external load (Equation 3).

$$i = \frac{V_b}{R_m + R_L} \qquad (3)$$

A voltmeter and ammeter connected as shown by the V and I circles determine the voltage and current of the external load (Figure 2b). Under finite R_L, total voltage is the summation of V_b and R_{int} (Equation 4).

$$V = V_b - iR_{\text{int}} \qquad (4)$$

When the fuel cell is operated as a hydrogen pump, Equations 2-4 are modified to take into account the external power supply to pump hydrogen from the anode to the cathode, as well as the competitive adsorption of impurities (such as CO) with H_2 at the anode.

Like the fuel cell, the power supply consists of a resistance (R_e) and voltage (V_{app}) that adjust to operate the pump (Figure 3). The applied voltage is in the opposite direction of V_b to supply current in the same direction as that of the fuel cell. When V_{app}= 0V, Figure 3 is the same as Figure 2.

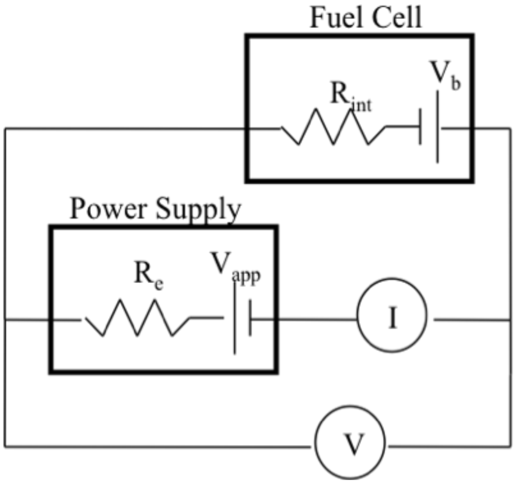

Figure 3. Circuitry of the hydrogen pump involving a fuel cell and power supply. It includes the fuel cell's battery voltage (V_b) and internal resistance (R_{int}), as well as the power supply's applied voltage (V_{app}) and external resistance (R_e). Voltage (V) and current (*i*) of the load can be detected via a voltmeter and ammeter, connected as shown by the V and I circles, respectively.

In the presence of the power supply, Equation 4 is modified to express the voltage across the load in relation to V_{app}, R_e, V_b, and R_{int} (Equation 5). R_e adjusts in response to the applied voltage to supply current.

$$V = V_b - iR_{\text{int}} = -V_{app} + iR_e \qquad (5)$$

CO affects the battery voltage, V_b, which reflects the chemical potential between the electrodes due to the catalytic oxidization of hydrogen at the electrode/electrolyte surface. The hydrogen activities at the electrodes are determined by the hydrogen partial pressures. Equation 6 details the reactions and components affecting hydrogen partial pressures at the electrodes. * refers to adsorption sites. K_H, K_{CO}, and K_W refer to the equilibrium constants of the reactions at each electrode. Θ indicates coverage of the indicated gas. Specifically, at the anode, CO and H_2 undergo competitive adsorption. At the cathode, an increase in oxygen leads to an increase in the oxygen partial pressure, which leads to a decrease in the hydrogen partial pressure, to yield higher V_b.

$$V_b = \frac{RT}{2\mathrm{F}} \ln \frac{P_{H_2}^{anode}}{P_{H_2}^{cathode}}$$

$$\text{ANODE:}$$

$$\text{with pure } H_2$$

$$2* + H_2 \rightarrow 2H* \quad K_H = \frac{(H*)^2}{(*^2)(P_{H_2})} \quad \theta_H = \frac{(K_H P_{H_2})^{1/2}}{1 + (K_H P_{H_2})^{1/2}}$$

$$\text{with } H_2 \text{ and } CO \qquad (6)$$

$$2* + H_2 \rightarrow 2H* \quad K_H = \frac{(H*)^2}{(*^2)(P_{H_2})} \quad \theta_H = \frac{(K_H P_{H_2})^{1/2}}{1 + (K_H P_{H_2})^{1/2} + K_{CO} P_{CO}}$$

$$* + CO \rightarrow CO* \quad K_{CO} = \frac{CO*}{(*)(P_{CO})} \quad \theta_{CO} = \frac{K_{CO} P_{CO}}{1 + (K_H P_{H_2})^{1/2} + K_{CO} P_{CO}}$$

$$\text{CATHODE :}$$

$$2H_2 + O_2 \rightarrow 2H_2\mathrm{O} \quad K_W = \frac{P_{H_2O}^2}{P_{O_2} P_{H_2}^2}$$

iii. Water's Importance

Water is an important factor affecting the fuel cell parameters because of its influence on the membrane resistance. Like a sponge, the membrane absorbs water to have sufficient water activity to promote the electrochemical reaction. From Equation 3, increased membrane water activity reduces the membrane resistance (R_m) to increase the current. However, too much water will block the diffusion of the reactants from the gas flow channels to the catalyst, reducing the active membrane area.

Lowered water activity results from an increase in external load resistance, temperature, and/or dry reactant flow rate. From Equation 3, an increase in external load resistance (R_L) decreases the fuel cell current, thereby decreasing water production and membrane water activity. The vapor pressure of water increases with temperature, resulting in more convective flow of water out of the fuel cell and reduced membrane water activity. Lastly, when the fuel cell is running on dry feeds, an increase in reactant flow rate dilutes the water concentration in the inlet streams and carries away water vapor, thereby reducing the membrane water activity. When the water activity is low, proton transport across the membrane is rate limiting; when the water activity is high, reactant transport from the gas flow channel to the catalyst surface becomes rate limiting. The two rate-limiting scenarios characterize the ohmic and mass transfer regions that will be discussed in 3e.

iv. Model Applications

The greatest utility of the STR PEM fuel cell is in the analysis of operating dynamics. By meeting the STR condition, the fuel cell model simplifies analysis by reducing compositional variations from studies on standard and hydrogen pumping operations, autohumidification, steady-state performance, and proton and reactant transport controls. This study is an example of utilizing the simplicity of an STR PEM fuel cell to explore hydrogen pumping for hydrogen purification. However, future work should consider the fuel cell as a plug flow reactor (PFR), which would allow larger reductions of hydrogen partial pressures between the anode and cathode to facilitate hydrogen pumping.

3. Experimental Methods

a. STR PEM Fuel Cell Design

Experiments were conducted with a custom-made STR PEM fuel cell. The blueprint is included in the Appendix. The inlet flow channels at the electrodes were 1/8" deep. They were fashioned into diamond-shaped graphite open gas plenums propped up by four pillars that applied equal pressure to the MEA. As explained in 2.c.i, the open gas plenum design with V_g~$0.2cm^3$ allows the PEM fuel cell to satisfy the STR condition at reactant flow rates between 1-20mL/min. Specifically, the residence times of gas in the plenums (τ_R=1.2-12s) were greater than the gas phase characteristic diffusion times (τ_D = 0.3-1s). The exception was when Q~75mL/min during hydrogen pumping; at high flow rates, the inlet gas was assumed well-mixed to preserve the STR condition. The active fuel cell area, where the gas and MEA contact, was ~$1.9cm^2$. Reactants entered horizontally into the inlets while water and unused reactants exited the outlets at a 45^oC tilt. The outlets allowed free drainage of liquid water by gravity to prevent water accumulation in the gas plenums and blockage of the gas diffusion layer.

Each plate making up the anode or cathode sides of a fuel cell consisted of a graphite block embedded in polyethylene, and an outer aluminum block. Earlier fuel cell plates employed in Prof. Benziger's lab used the more malleable teflon rather than polyethylene to embed the graphite block. However, since teflon deformed more easily at higher temperatures and pressures, it was replaced with polyethylene for this study. A better material to consider for operations over

100^{o}C would be polycarbonate. A copper foil current collector connected to the external circuit was placed in-between the graphite and polyethylene blocks. Silicon-coated fiberglass gaskets were placed in-between the polyethylene and aluminum blocks for insulation and sealing.

The assembled STR PEM fuel cell consisted of two fuel cell plates making up the anode and cathode sides, and was tightened with four bolts applied at ~5Nm of torque (Figure 3). Holes for the thermocouple and cartridge heaters were placed within the aluminum blocks.

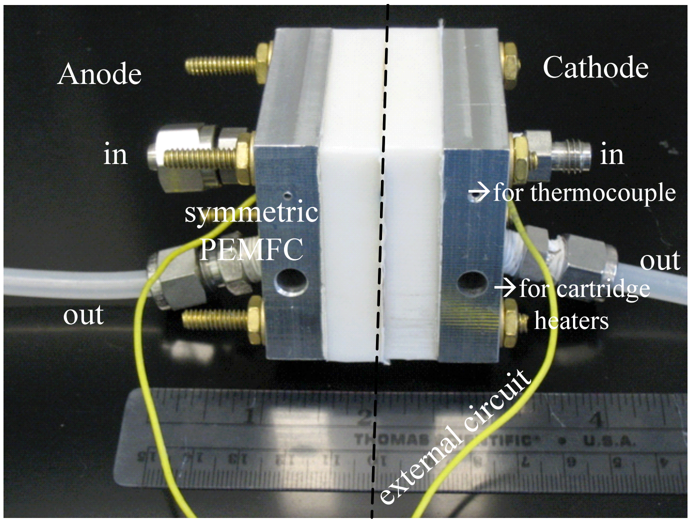

Figure 4. Photograph of an assembled STR PEM fuel cell. Relevant parts are labeled.

b. Synthesis of the Membrane Electrolyte Assembly (MEA)

A variety of polymer membranes can be assembled to make a PEM fuel cell. This study employed a custom-made Nafion/carbon-cloth membrane electrolyte assembly (MEA). The MEA included a Nafion^{TM} 115 membrane (Ion Power, Inc., DE, USA) pressed between 2 E-TEK electrodes (A6 ELAT, DeNora, NJ, USA) that consisted of carbon cloth on one side and Pt catalyst on the other side. Nafion is the proton conductor. Carbon cloth serves as the gas diffusion layer. Nafion is a perfluorosulfonated polymer that was cleaned prior to MEA application via one-hour sequential boilings in 3wt% H_2O_2, DI water, 1M sulfuric acid, and DI water, respectively. The catalyst weight loading was ~0.4mg Pt/cm^2. The MEA was prepared by coating Pt catalyst sides of two electrodes with 5wt% Nafion in solution to a loading of ~0.6mg-Nafion/cm^2; the coating served to improve the three-phase interface between electrolyte, catalyst, and reactant gas at both the anode and cathode [9]. After baking at 70^{o}C to drive off alcohol, the electrodes were framed inside silicon-coated fiberglass gaskets, and pressed against a Nafion 115 membrane via hot press at 140^{o}C and 20 MPa for 90s. Four bolt holes were placed in the gasket section of the MEA. The MEA was stored in 100% relative humidifier tanks overnight prior to use (Figure 5).

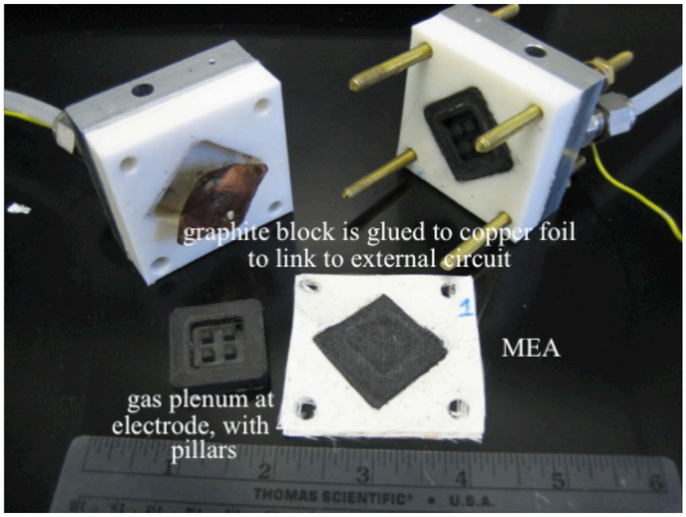

Figure 5. Photograph of MEA and related parts. The MEA is sandwiched between two symmetric electrode plates consisting each of graphite (with gas plenum), copper foil current collector linked to the external circuit (yellow wire), and polyethylene and aluminum outer blocks. Four bolt holes in the MEA gasket section allows MEA insertion into the fuel cell without sacrificing sealing.

c. Setup Materials

Figure 6 shows the experimental setup and materials. Hydrogen (H_2), oxygen (O_2), nitrogen (N_2), and carbon dioxide (CO_2) input streams were provided by commercial cylinders (Airgas, Inc.) and were regulated by either hydrogen or oxygen mass flow controllers (Aalborg Instruments) with flow rate ranges 0-50mL/min. The controllers were manually adjusted. The fuel cell's outlet tubes were submerged in water baths at room temperature to collect liquid water, detect bubbling via a bubblemeter, and prevent back-diffusion of air. The fuel cell temperature was measured and controlled via thermocouple and cartridge heaters that were inserted into the aluminum blocks. A humidifier tank wrapped and insulated in heating tape served to heat and humidify the inlet streams; a thermocouple at the external base of the humidifier tank determined the approximate water temperature in the tank. The water content of the inlet stream was measured via a Sensiron SHT7X (Sensiron AG, Switzerland) digital temperature and humidity sensor linked to the HumiViewer computer program. When the fuel cell was heated, it was mounted inside an insulated temperature-controlled aluminum box to establish temperature uniformity. The fuel cell circuit was completed by connecting the anode and cathode external circuits to a short wire or to Arbin Instruments (TX, USA), which runs a MSTAT4+ software.

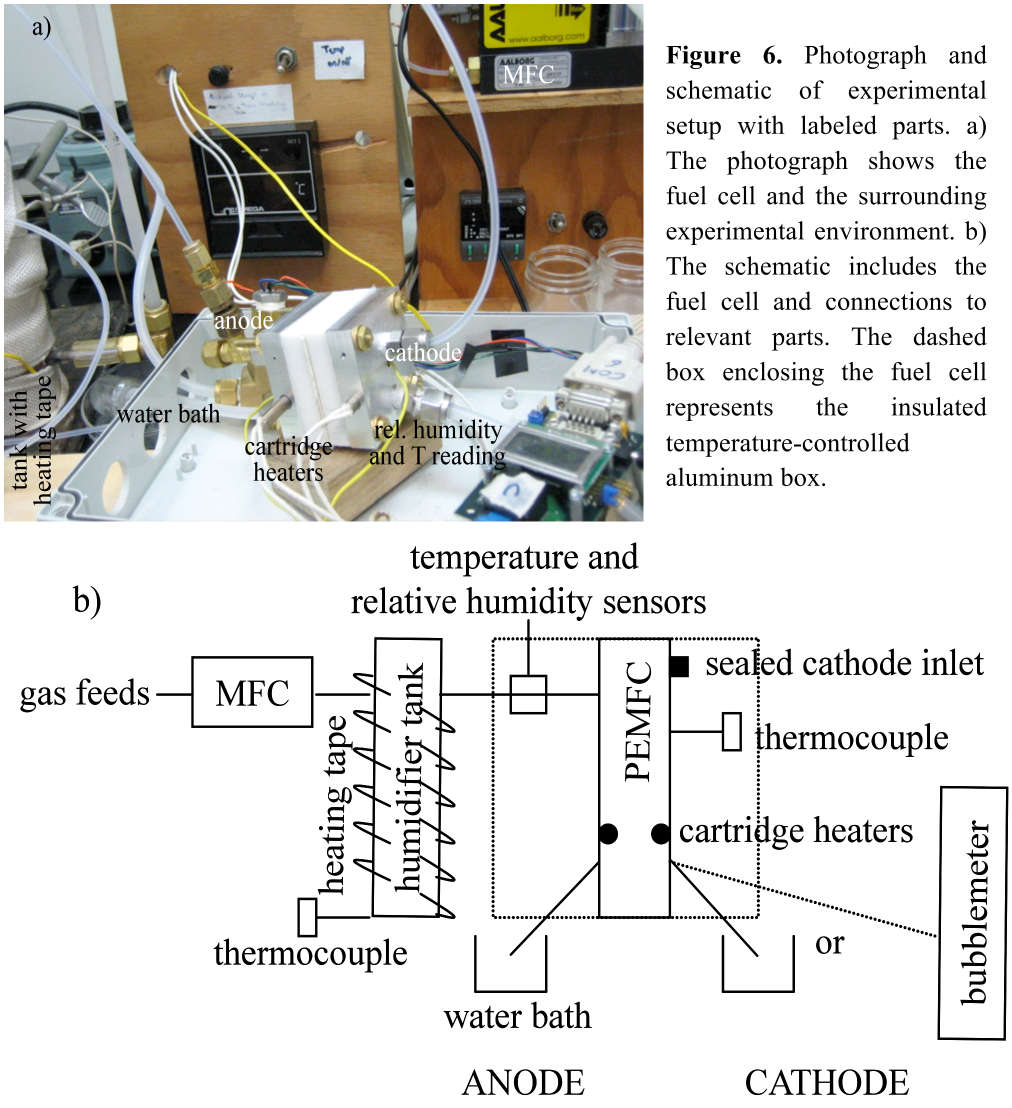

Figure 6. Photograph and schematic of experimental setup with labeled parts. a) The photograph shows the fuel cell and the surrounding experimental environment. b) The schematic includes the fuel cell and connections to relevant parts. The dashed box enclosing the fuel cell represents the insulated temperature-controlled aluminum box.

d. Potentiostatic PEM Fuel Cell Manual Operation Setup

Potentiostatic operation varies the external load (independent system variable) of the STR PEM fuel cell to change current. Potentiostatic operations are voltage-controlled since voltage across the load impedance is fixed. The internal resistance of the custom-made MEA can be read from the resulting power performance curve. The STR PEM fuel cell was run as a hydrogen fuel cell with hydrogen at the anode inlet and oxygen at the cathode inlet. The fuel cell was connected to an ammeter and a 10-turn, 0-20 Ω, 6W potentiometer in series, and a voltmeter in parallel (Figure 7).

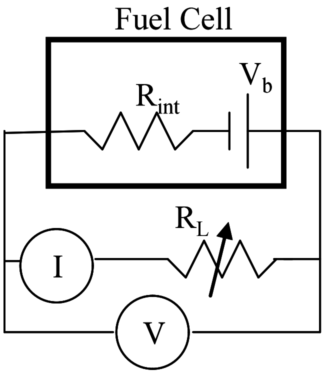

Figure 7. Schematic of fuel cell circuitry under potentiostatic operation. The potentiostatic operation utilizes a 10-turn 0-20 Ω, 6W potentiometer, ammeter, and voltmeter.

The power performance curve sets power as a dependent system variable and the external load as an independent system variable. In literature, the power performance curve was obtained by transforming experimental and model data from a polarization (IV) curve for a 1.3cm^2 PEM fuel cell employing ETEK electrodes pressed against a Nafion 115 membrane [11]. Three operating ranges were detected when the external load varied from 0 to ∞ Ω. Figure 8 reproduces the data courtesy of Benziger *et al* [11]. The three operating ranges are explained in detail in 3e.

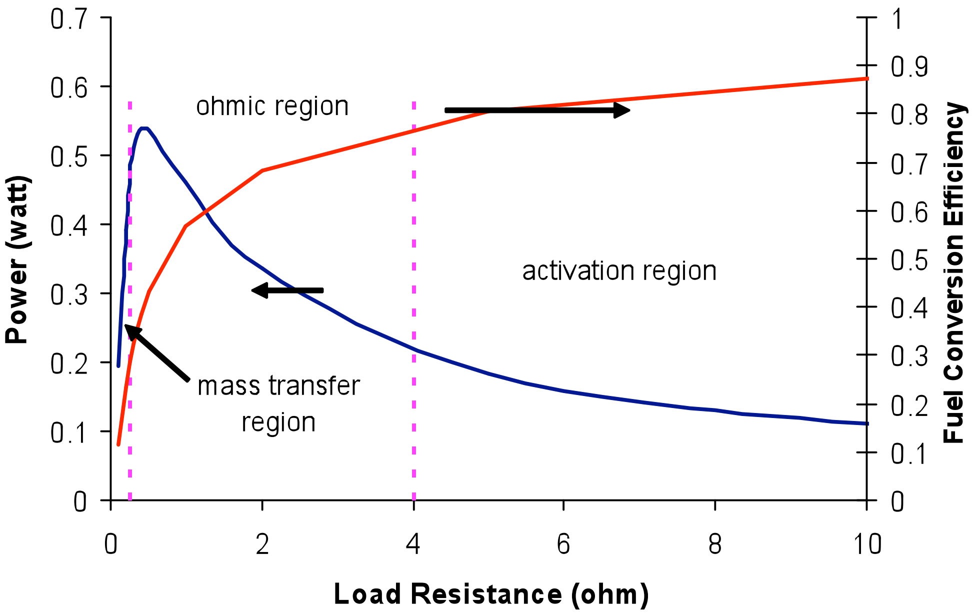

Figure 8. Power performance curve of a STR PEM fuel cell under standard hydrogen fuel cell operation. The graph is reproduced from Benziger *et al* [11]. The three operating ranges are the activation, ohmic, and mass transfer regions.

The power performance curve plots power (P) against load resistance ($R_L = V/i$). The power for a resistive external load is given by Equation 7; it is differentiated to determine P_{max} in Equation 8. At P_{max}, $R_L = R_{int}$ so the power performance curve can be used to determine an MEA's internal resistance.

$$P = \frac{V_b^2 R_L}{(R_{\text{int}} + R_L)^2} \qquad (7)$$

$$P_{\max} = \frac{V_b^2}{4R_L} \qquad at \qquad R_L = R_{\text{int}} \qquad (8)$$

e. Galvanostatic PEM Fuel Cell Manual Operation Setup

Voltage and resistance of the power supply are varied to maintain the current at fixed values for galvanostatic operation. Galvanostatic operations are therefore current-controlled. When an external power supply applies current (increase in *i*) to pump hydrogen from the anode to the cathode, Equation 4 indicates that the voltage of the external load becomes negative. Hydrogen pumping serves as the basis for hydrogen purification since past the greater of the residence (τ_R) and diffusion (τ_D) times of impure gases in the cathode outlet gas stream, the resulting gas will be pure hydrogen. The STR PEM fuel cell was connected to a HP 6114A Precision Power Supply and an ammeter in series, and a voltmeter in parallel to obtain a polarization (or IV) curve (Figure 9).

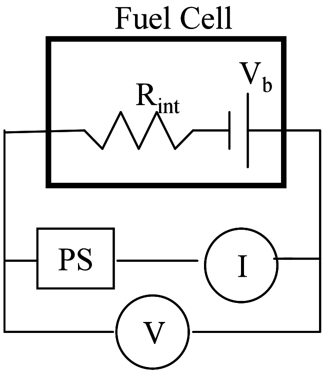

Figure 9. Schematic of fuel cell circuitry under galvanostatic operation. The galvanostatic operation utilizes a HP 6114A Precision Power Supply, ammeter, and voltmeter.

In literature, the polarization (or IV) curve was obtained experimentally by varying the external load and plotting voltage against current. Data from Benziger *et al* [11] using the same $1.3 cm^2$ PEM fuel cell as discussed in 3d. is reproduced to show the three operating ranges when the external load varied from 0 to ∞ Ω

(Figure 10). A theoretical IV curve derived from Equations 2-4 via model parameters corresponded to the experimental data.

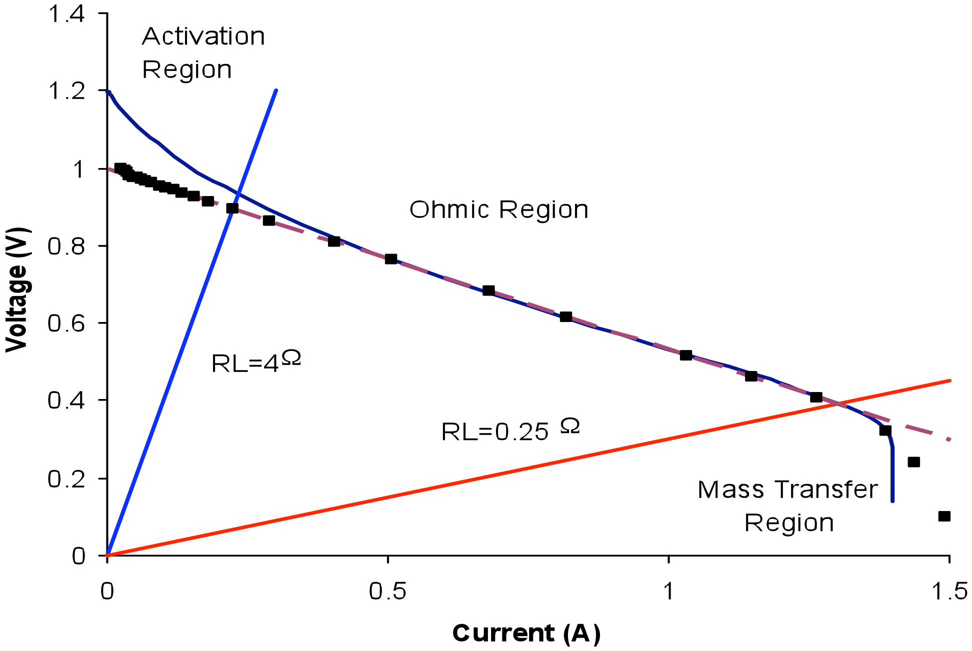

Figure 10. Polarization (IV) curve of a STR PEM fuel cell under standard hydrogen fuel cell operation. The graph is reproduced from Benziger *et al* [11]. Experimental data is represented as square markers; modeled data is represented as a solid line. The three operating ranges are the activation, ohmic, and mass transfer regions.

The IV curve theorized that without hydrogen crossover from the anode to the cathode, the open circuit voltage, which was determined at 0A and ∞ Ω, was 1.2V. The three operating polarization ranges were the activation (i<0.2A), ohmic (0.2A<i<1.25A), and mass transfer (~1.45A) regions [11]. The activation region was reached at external load resistance R_L>4Ω. The electron transfer barrier on the electrode/electrolyte interface decreased voltage in the activation region [11]. The ohmic region, the most common operating range for a fuel cell, was reached at external load resistance 4Ω>R_L>0.25Ω. An increase in membrane resistance

(R_{int}) resulting from low membrane water activity or disturbances of the three-phase interface between electrolyte, catalyst, and reactant gas limits current and voltage in the ohmic region [11]. The negative slope of the IV curve in the ohmic region is the R_{int} and the y-intercept is V_b as stated in Equation 4. The reactant gas rate of diffusion from the gas flow channels to the catalyst surface limits current and voltage in the mass transfer region; its role is characterized in Equation 2 [11].

f. Arbin Setup

The potentiostatic and galvanostatic PEM fuel cell operations were conducted manually by physically increasing the potentiometer's resistance or the power supply's voltage and resistance. The Arbin Instruments MSTAT4+ software automated the two procedures via custom-made schedules detailing desired fuel cell operations. The Arbin schedules that were predominately used determined open circuit voltage (OCV) and fuel cell response to hydrogen pumping via current sweep (CS). OCV and CS sample schedules are included in the Appendix. Schedules determined internal resistances in pulses. Once the schedules proved capable of reproducing manual data, Arbin became the dominant experimental setup.

Arbin had some quirks that made data appear inconsistent. The fuel cell's voltage via Arbin's OCV schedule was always different in sign from that of the resting step of Arbin's CS schedule. The OCV schedule recorded voltage with a positive sign while the CS schedule recorded voltage with a negative sign. An explanation is that although a fuel cell under hydrogen pumping in the absence of O_2 cannot generate current, the difference in hydrogen partial pressures at the electrodes results in positive voltage (Equation 6). Arbin's OCV schedule detects this potential difference as a positive voltage reading, but Arbin's CS schedule, which controls current, could have supplied its own current in order to detect a current reading. According to Equation 4, the applied current yielded a negative voltage reading.

g. Hydrogen Pumping Setup

As a hydrogen pump, the fuel cell's cathode inlet was sealed while the anode inlet was injected with dry or humidified H_2/N_2 or H_2/CO_2 gas streams. The anode and cathode outlets were immersed in water baths. During current sweeps, when hydrogen was detected at the cathode outlet, a bubblemeter was connected to measure the gas flow rate. The humidifier tank was heated with heating tape and its water temperature was approximated by a thermocouple at the tank's external base. The humidifier works by immersing an inlet stream of dry gas in water. Gas bubbles out of the water and into the outlet to form the humidified gas stream entering the fuel cell's anode inlet. The relative humidity of the inlet gas stream was measured via a Sensiron SHT7X (Sensiron AG, Switzerland) digital temperature and humidity sensor linked to the HumiViewer computer program (Figure 11).

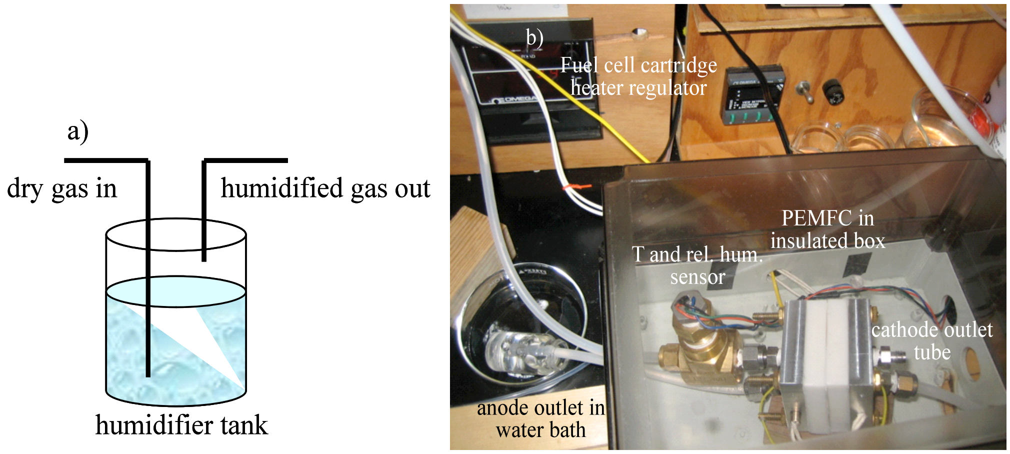

Figure 11. Diagram of the humidifier tank and photograph of the hydrogen pump that employs the tank. a) Anatomy of the inside of the humidifier tank reveals the positions of the dry and humidified gas streams. b) Photograph shows the hydrogen pump with labeled parts.

h. Limitations on Experimental Setup

There was an unexpected backflushing of humidifier tank water into the mass flow rate gas controllers when setting up for hydrogen pumping via H_2/N_2 and H_2/CO_2 inlet streams. The cause is most likely attributed to a buildup of tank pressure due to blockage of gas in the fuel cell. The flooded mass flow controllers led to imprecise flow rate readings. Due to time constraints, the mass flow controllers were not sent back to Aalborg Instruments to be fixed. They were dried and fixed as much as possible in lab. Although the “fixed” mass flow rates deliver steady flow, they act more like on/off switches than flow controllers. Faulty mass flow controllers will limit the accuracy of the experimental data but given the emphasis on the hydrogen pumping phenomenon rather than on quantitative details, the consistent flow rate with backup bubblemeter readings were adequate for the experiments.

The cartridge heaters were much more responsive to temperature set point than was the humidifier tank to the heating tape. This results in a fast heating time of the fuel cell and a gradual heating time of the tank's water. Since the membrane water activity is affected by both the amount of water carried through the feed (affected by the tank's temperature) and the fuel cell's temperature (affected by the cartridge heaters), the greater power of the heating cartridges meant a faster drying out of the MEA before humidified feed could reach it. As the fuel cell temperature increased, the relative humidity of the anode inlet stream decreased. The experimental setup can be improved with equal-powered heaters with temperature control at the tank and fuel cell, and insulated tubing extending from the tank outlet to the fuel cell inlet.

The Arbin program has a safety mechanism to shut off schedules when the voltage reaches beyond $|\pm 5V|$. The regulation meant that the fuel cell was unable to maintain the desired current long enough to collect a steady gas stream from the cathode outlet before the schedules terminated. The problem could be circumvented in future work in four ways: change Arbin's safety voltage limit to a greater magnitude, employ commercial MEA using Nafion 112 to increase the fuel cell's current density (to prevent overall voltage from reaching Arbin's limit), optimize the relative humidity of the inlet stream to prevent drying out of the MEA, or forgo the automated Arbin setup for the galvanostatic manual setup.

Evidence of cracked graphite blocks in earlier STR PEM fuel cells in lab indicate that solid graphite is not ideal for withstanding some combination of high pressure, high temperature, and minimal water concentration. Future STR PEM fuel cell designs could find the optimal ratio of powdered graphite to conductive epoxy to create graphite blocks not subject to cracking. Graphite blocks did not crack for the custom-made STR PEM fuel cell employed in this study.

4. Results and Discussion

a. Potentiostatic PEM Fuel Cell Manual Operation Tests

A STR PEM fuel cell under standard stoichiometric $10H_2/5O_2$ fuel cell feeds underwent potentiostatic operation that varied external load from 0-20 Ω in 60s. Variations in membrane water activity shifted the power performance curves produced on different days, while preserving the same curvature (Figure 12). The fast sweep in external load resistance ensured that the membrane water activity remained constant during each experiment. Maximum power was obtained at the lowest load resistance, which as addressed in 3d is also the internal resistance. Despite variations in the membrane water activity on different days, the power performance curves yielded the same order of magnitude of internal resistance $\leq$ 1.58Ω (internal resistance is the load resistance intersecting the dashed line). The open circuit voltage measured before each run was $\geq$ 0.80V. These values corresponded with literature [11]. Low internal resistance reflected good three-phase interface between electrolyte, catalyst, and reactant gas, and sufficient membrane water activity.

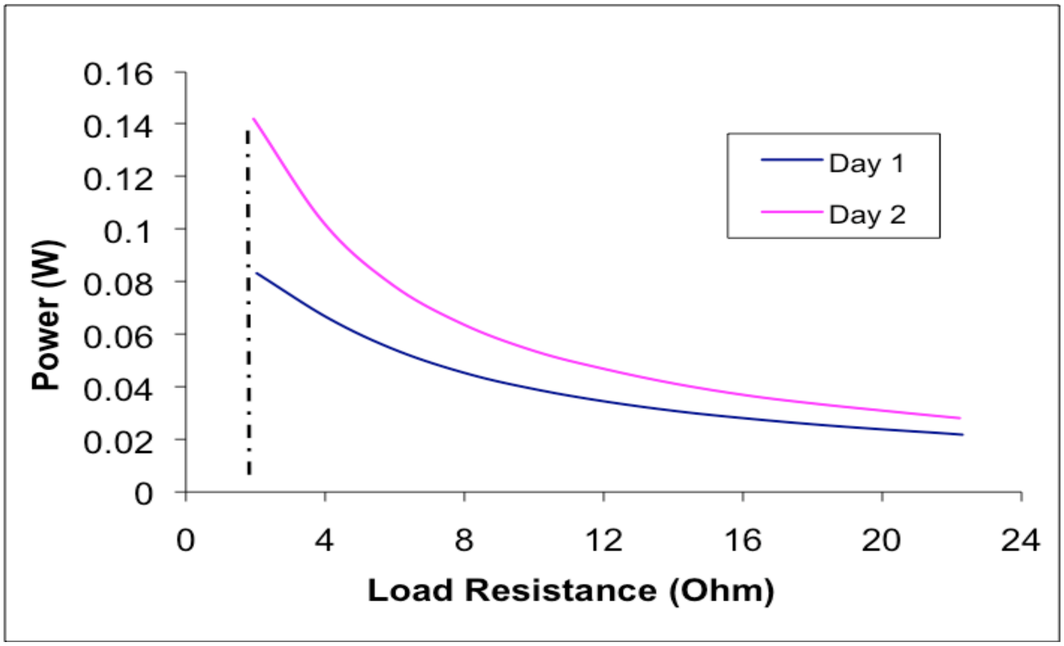

Figure 12. Power performance curve of a fast sweep potentiostatic operation under standard hydrogen fuel cell feed. The sweep lasts ~60s under stoichiometric $10H_2/5O_2$ inlet gas streams. The R_L reading at the dashed line determines the R_{int}.

b. Galvanostatic PEM Fuel Cell Manual Operation Tests

IV curves were generated from galvanostatic operation by varying resistance and voltage of a HP 6114A Precision Power Supply at various hydrogen and oxygen feed flow rates (Figure 13). Depending on reactant availability, the fuel cell first generated its own current (up to ~0.13A) before the power supply provided more. Rate of current increase was ~10mA/s. The power supply varied its resistance in response to increases in its voltage to sustain the applied current. The overall voltage decreases as more current is supplied (Equation 4). The IV curve is therefore downward sloping with voltage shifting in sign from positive to negative as current is applied.

O_2 bubbling at the cathode outlet stream ceased as voltage turned negative to indicate that it became the limiting reactant. As expected, at increasing O_2 flow rates to the cathode inlet, the fuel cell's V_b also increased (Equation 6) such that the power supply applied less current. Figure 13 reflects this trend with a rightward shift in IV curves at higher O_2 flow rates. All three galvanostatic runs shares approximately the same curvature. The runs with $10H_2/10O_2$ and $10H_2/5O_2$ generated almost identical data (disregarding the high-slope voltage region between 0.4-0.6A). The similarity of these two data sets makes sense since the reactions in both runs preserved the stoichiometric $10H_2/5O_2$ condition with H_2 as the limiting reactant in the $10H_2/10O_2$ run and O_2 as the limiting reactant in the $10H_2/5O_2$ run.

Because the IV curves were swept in a time period <100s, the membrane water activity (and the internal resistance) could be assumed constant. At 0mL/min O_2 flow rate, if a current was not applied to pump hydrogen, water from the water bath might enter the fuel cell via the cathode outlet. The experiment did not observe this situation, which indicated that the overall fuel cell system was at atmospheric pressure to counter the pressure exerted by air at the surface of the water bath. The fuel cell setup was monitored to prevent water back-up into the fuel cell as it would block the gas diffusion layer, flood the MEA, and reduce the active membrane area, thereby leading to decreased current.

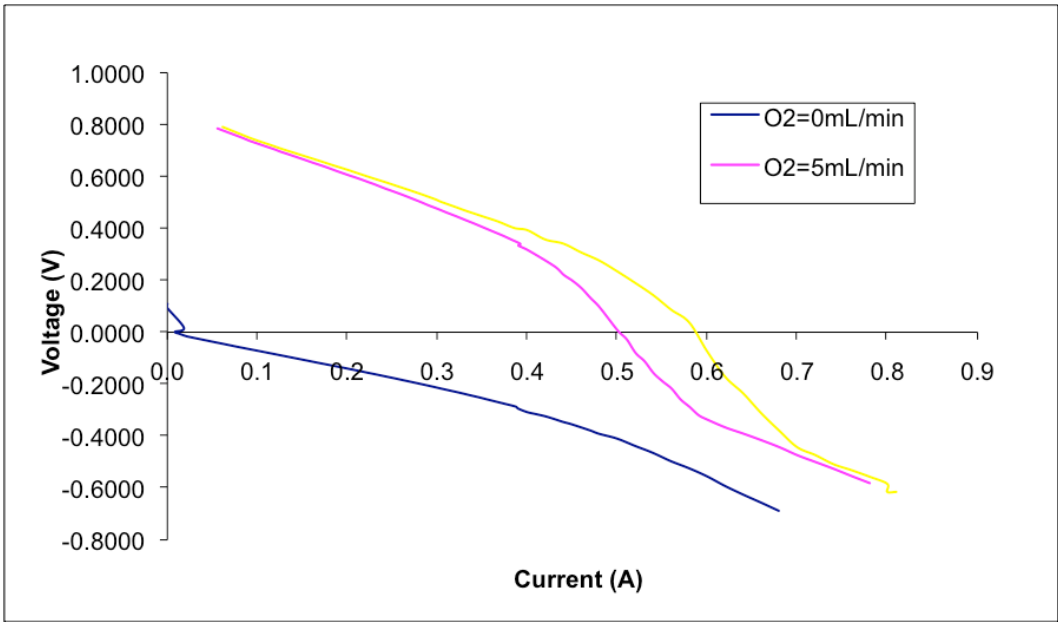

Figure 13. IV curves at different H_2/O_2 gas stream ratios. The curves were generated in <100s at constant H_2= 10mL/min in the anode inlet and varying O_2= 0, 5, and 10mL/min in the cathode inlet.

The initial positive voltage at the $10H_2/0O_2$ run was most likely confounded by the presence of leftover O_2 from the other runs. The expected potential difference is zero since there is no hydrogen partial pressure difference between the electrodes given H_2 crossover with no O_2 to utilize the crossover.

c. Reproducing Manual Operation Tests on Arbin

The Arbin Instruments MSTAT4+ software reproduced galvanostatic operation manual tests runs with H_2/O_2 feeds (Figure 14). As expected, Arbin mirrored its own runs the closest. Both the manual and Arbin results indicated a high-slope voltage region from 0.4-0.7A. The high-slope voltage region is investigated with more experiments and discussed in more detail in 4.d.iv.

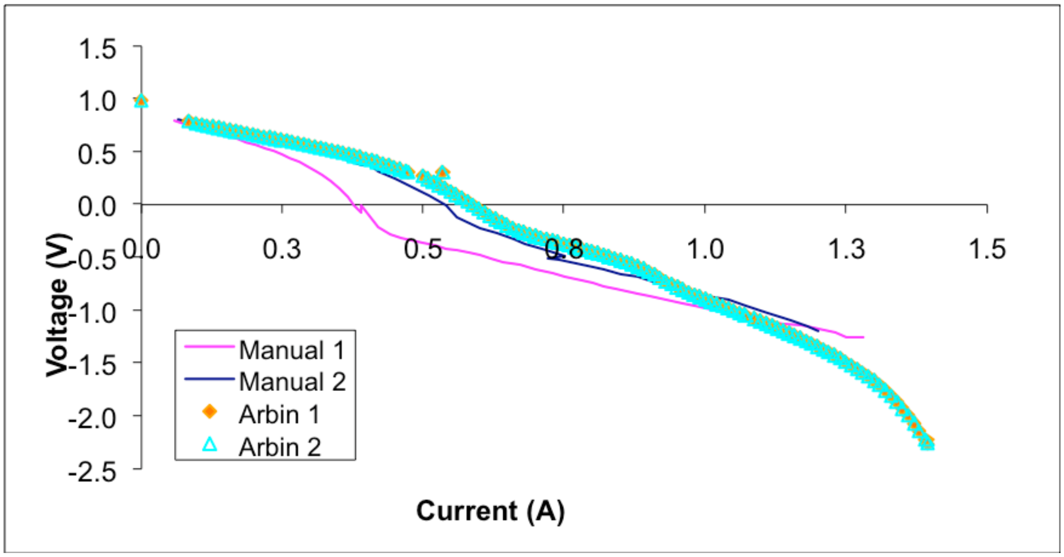

Figure 14. Reproducing manual runs on Arbin. All runs were conducted under the same standard operation with $10H_2/5O_2$ inlet gas streams. As expected, Arbin mirrored its own runs almost perfectly. The Arbin tests incorporated markers in order to better reveal the overlapping of its two data sets.

d. Hydrogen Pumping Tests

i. H_2/N_2 Current Sweep

The hydrogen pump utilized dry H_2/N_2 anode inlet streams to analyze changes to the IV curve at varied current sweep rates. The cathode inlet was sealed and the anode and cathode outlets were immersed in water baths. After verifying that the H_2/N_2 inlet stream yielded open circuit voltage and internal resistance on the same order of magnitude as standard H_2/O_2 runs, a manual galvanostatic run was conducted. The power supply utilized up to 3V to apply current to pump hydrogen from the anode to the cathode. The gas flow rate at the cathode outlet (6.9ml/min) deviated from the theoretical flow rate (7.6ml/min) by 9.21%. Calculations are based on Equation 10 found later in this section and can be reviewed in 4.d.iv. The lower experimental H_2 flow rate was expected since imperfect sealing and crossover of hydrogen from the anode to the cathode reduced reactant availability to generate more hydrogen flow at the cathode outlet.

Arbin results on fuel cell runs with dry H_2/N_2 inlet ratios ranging from 0.2-1 showed the expected trend of pumping more hydrogen given more H_2 at the anode inlet (Figure 15). The result was an increased rightward shift in IV curves.

Figure 15 also showed the effect of H_2/N_2 fuel cell operation at different current sweeps (0.01A/s and 0.002A/s). As expected, results at the lower current sweep rate made the activation, ohmic, and mass transfer regions more pronounced.

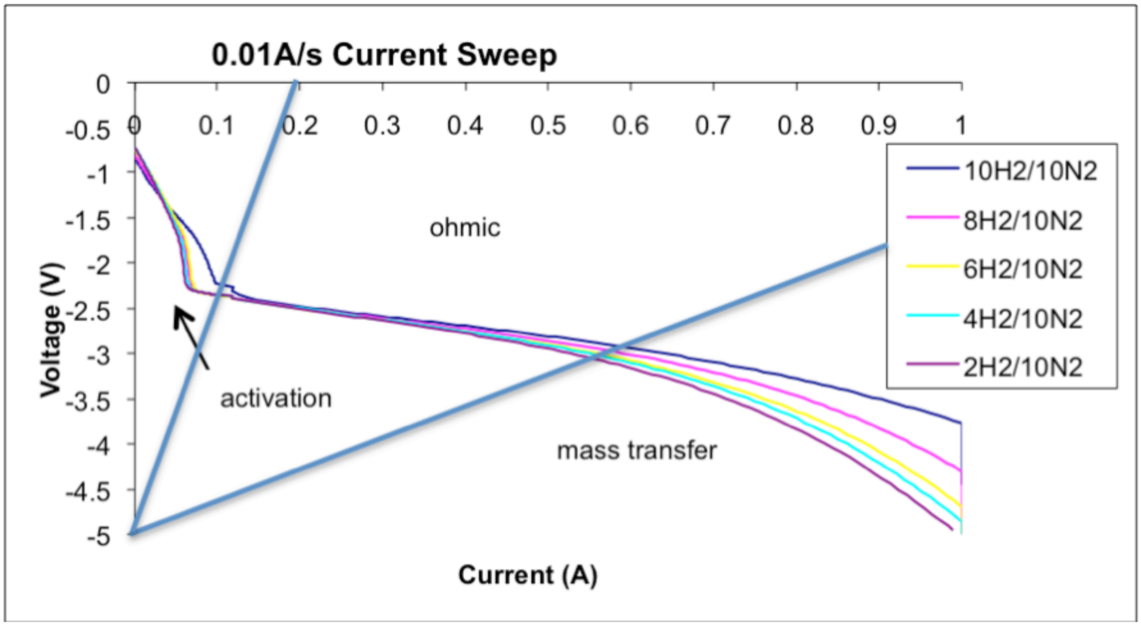

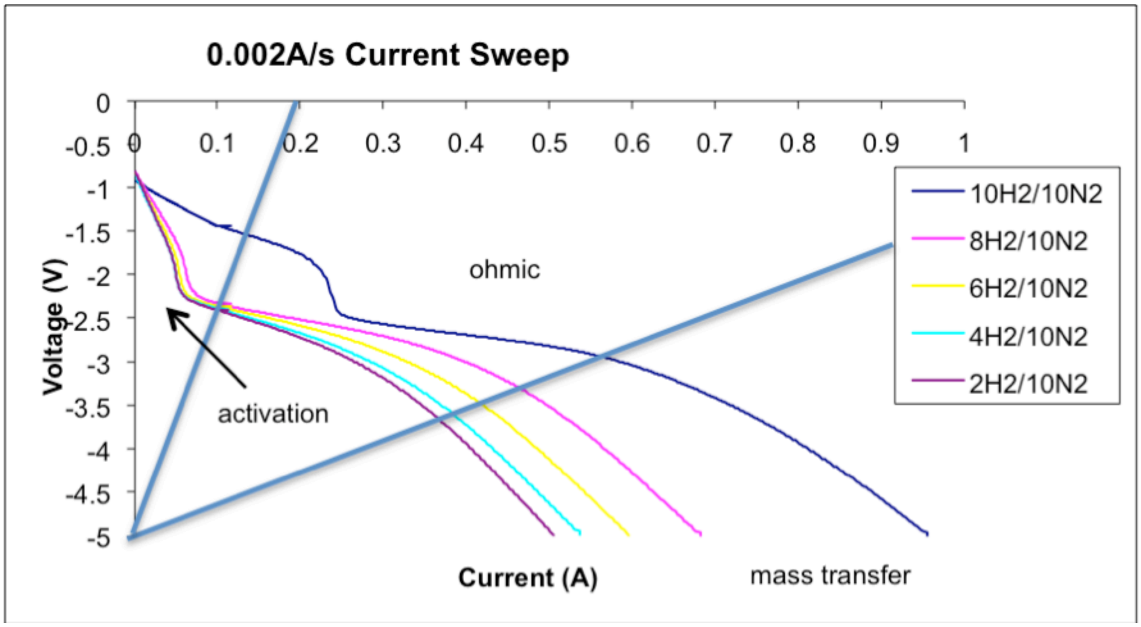

Figure 15. IV curve of hydrogen pumping under different current sweep rates. Hydrogen pumping utilized varying dry H_2/N_2 inlet gas streams. The activation, ohmic, and mass transfer regions are more pronounced (more spread out) at the slower sweep rate of 0.002A/s.

The gas flow channels act as reactant reservoirs. Equation 9 characterizes the reservoir's overall H_2 mole balance. As a hydrogen pump with a sealed cathode inlet, Q_C^{in} = 0mL/min. At steady state, Equation 9 simplifies to Equation 10, which equals the total amount of moles of H_2. Equation 10 can be used to predict gas flow rate at the cathode outlet given the current. Section 4.d.iv includes a list of theoretical flow rates calculated at given experimental temperatures and currents. Slight modifications to these equations can be applied to oxygen when it is injected into the cathode inlet.

$$\frac{V_C}{RT}\frac{\partial P_{H_2}^{out}}{\partial t} = \frac{Q_C^{in}P_{H_2}^{in} - Q_C^{out}P_{H_2}^{out}}{RT} - {}^{i}\!/_{2F} \qquad (9)$$

$$moles = feed - removal$$

$$n = \frac{i}{2\mathrm{F}} = \frac{Q_C^{out} P_{H_2}^{out}}{RT} \qquad (10)$$

One difference between the IV curves produced under standard and hydrogen pumping operations was the initial voltage sign at low current. Unlike the IV curve of the $10H_2/0O_2$ current sweep (Figure 13), the hydrogen pump's current sweeps started at negative voltage. As addressed in 4b, positive voltage might be caused by residual O_2 at the cathode inlet from previous runs. Without the residual O_2 present, both operations should display zero or negative voltage at the start of the current sweep.

Another difference is the amount of voltage Arbin's power supply applied in order to reach desired current under standard and hydrogen pumping operations. There is no current output from a PEM fuel cell in the absence of O_2. When the cathode inlet was sealed and an inert (N_2) was injected into the anode inlet, there was low fuel cell performance. Assuming STR conditions with no spatial compositional variations in the PEM fuel cell, inert gas restricted reactant mass transport in the gas diffusion layer. Figures 13 and 15 reflected low current output in the absence of O_2. They indicated that the fuel cell supplied its own current only in the H_2/O_2 run to yield an overall higher voltage of -0.6V. Since the fuel cell relied on the power supply to apply current in the H_2/N_2 run, the overall voltage was lower, at -3V.

Since the two graphs in Figure 15 utilized data taken over a month apart with different hand-made MEAs, the results should be viewed more for qualitative than quantitative considerations. The data could be confounded by

MEA quality and membrane water activity level. However, the preservation of the general trend, minus idiosyncrasies such as the extreme rightward shift at lower current regions on the $10H_2/10N_2$ run at current sweep 0.002A/s, reflected that the fuel cell behaved consistently as a hydrogen pump.

ii. Humidified Feeds

The fuel cell feeds for hydrogen pumping were passed through a humidifier tank to prevent the membrane from drying out in the absence of O_2. Dry H_2/N_2 and H_2/CO_2 streams passed through a humidifier tank before entering the anode inlet. Temperatures of the tank and the fuel cell were varied to increase the relative humidity of the feeds and to decrease catalyst poisoning by CO_2. The ideal was to maintain 80-100% relative humidity of the feeds to hydrate the membrane without blocking gas diffusion.

The feed flow rate of H_2/N_2 and H_2/CO_2 were ~75mL/min. Under the high flow rate, the fuel cell no longer satisfied the STR condition since it led to $\tau_R \leq 0.002s < \tau_D$ (the residence time was less than the diffusion time to the catalyst). The setup incorporated high H_2 flow rates at the anode to allow for larger reduction of hydrogen partial pressures at the anode and cathode to facilitate hydrogen pumping. The large percentage of H_2 in the anode inlet stream also aimed to roughly imitate the industrial H_2 stream needing purification. The tank temperature affected the relative humidity of the feeds, which in turn affected the internal resistance of the membrane.

When both the tank and fuel cell temperatures were adjusted, the combination of $60H_2/15CO_2$ runs yielding the highest open circuit voltage and the lowest internal resistance was fuel cell at 25^oC and tank at 55^oC (Figure 16a). The temperature labels below the title on both graphs of Figure 16 indicate the fuel cell temperatures. For the runs, there is no sensitivity of open circuit voltage to internal resistance since the membrane resistance is much less than ∞ Ω. The fact that higher fuel cell temperatures neither maintained humidity of the inlet streams nor improved fuel cell voltage via decreased CO_2 poisoning was unexpected. An explanation is that fuel cells at higher temperatures counteracted the effect of the humidifier tank by drying out the humidified feeds, thereby drying out the membrane and increase internal resistance. A corresponding time plot of relative humidity of the inlet stream and internal resistance supported this explanation (Figure 16b).

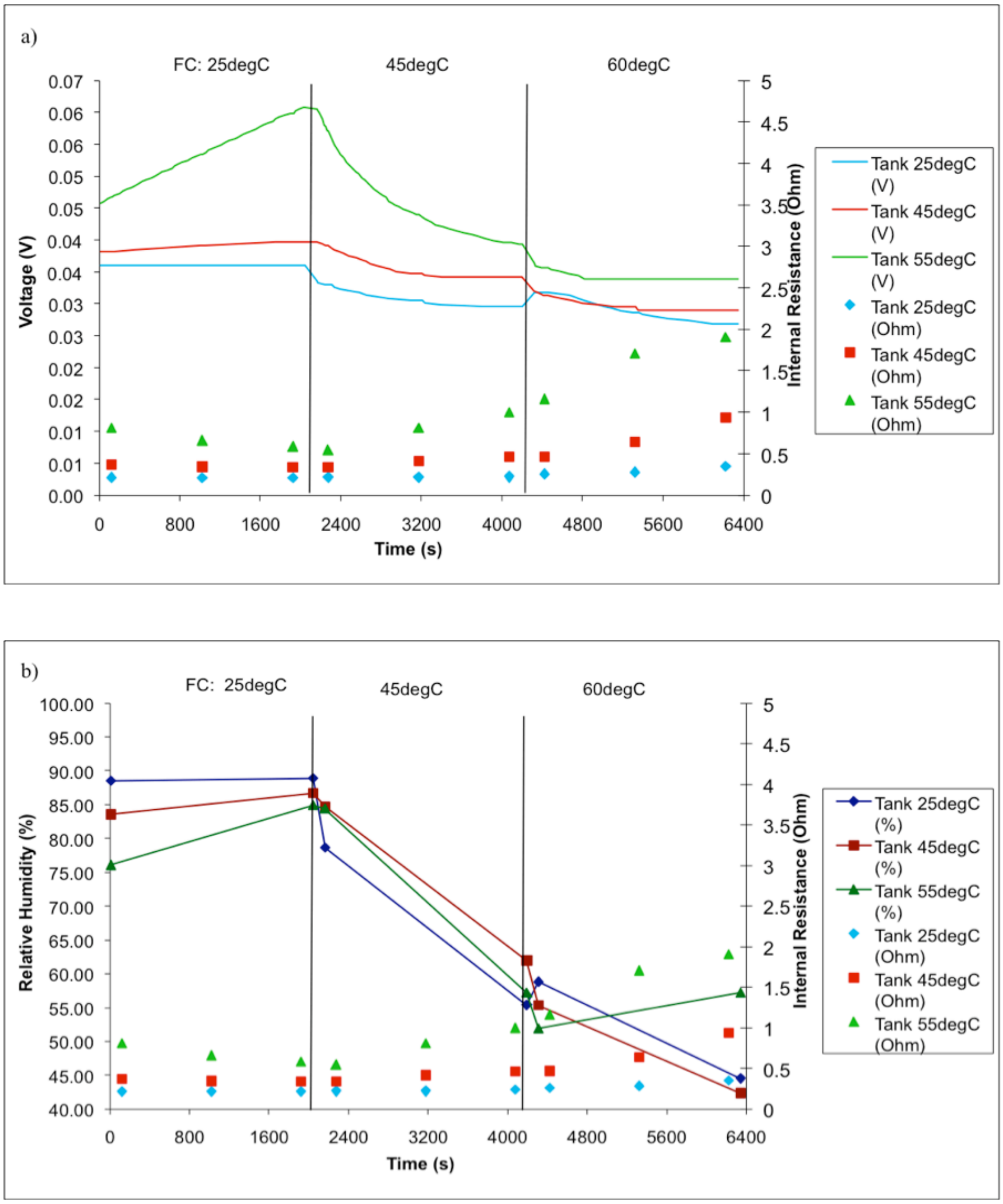

Figure 16. Effect of temperature change on $60H_2/15CO_2$ hydrogen pumping. The humidifier tank's temperature was set to 25, 45, and 55^{o}C (see legend). The fuel cell's temperature was set to 25, 45, and 60^{o}C (see top of graph). a) Open circuit voltage runs on humidified H_2/CO_2 at varying temperatures indicates maximum voltage with fuel cell at 25^{o}C and tank at 55^{o}C. b) A corresponding time plot indicates the relative humidity of the inlet stream and the internal resistance.

Figure 16a showed a peculiar upward open circuit voltage increase with fuel cell at 25^{o}C and tank at 55^{o}C. With the hydrogen fuel cell running as a hydrogen pump, it was unclear why the absence of O_2 caused an increase in voltage. Since low tank temperatures presumably carried less water vapor into the fuel cell to yield low relative humidity, finding lowest internal resistances at the lowest tank temperature was unexpected. The curve with varying fuel cell temperatures and tank at 55°C were repeated with H_2/CO_2 as well as with H_2/N_2 at the same flow rates to investigate the upward peculiarity on open circuit voltage (Figure 17a). A time plot of relative humidity and internal resistance was included (Figure 17b).

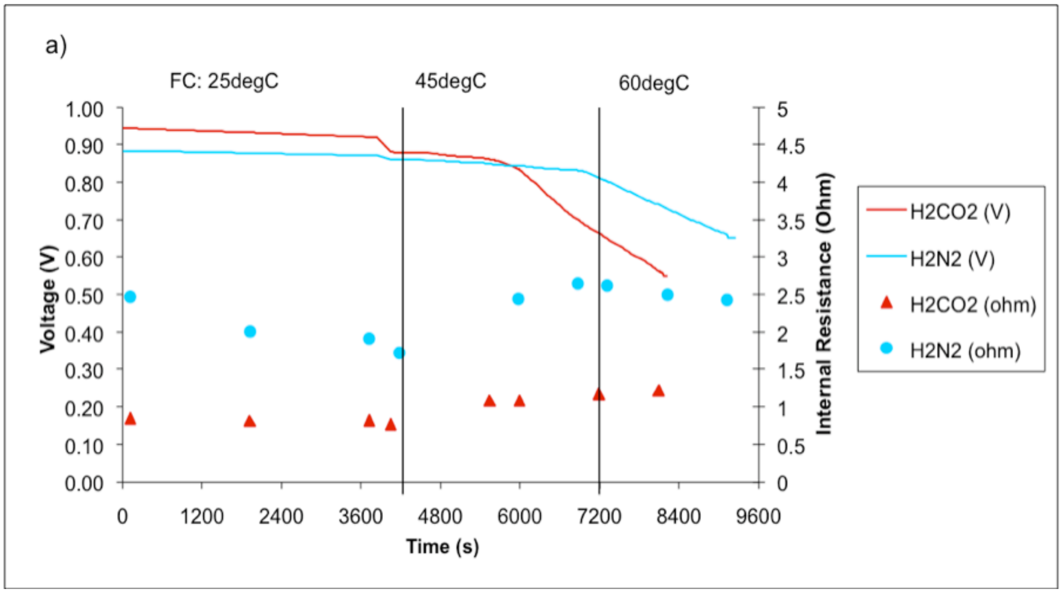

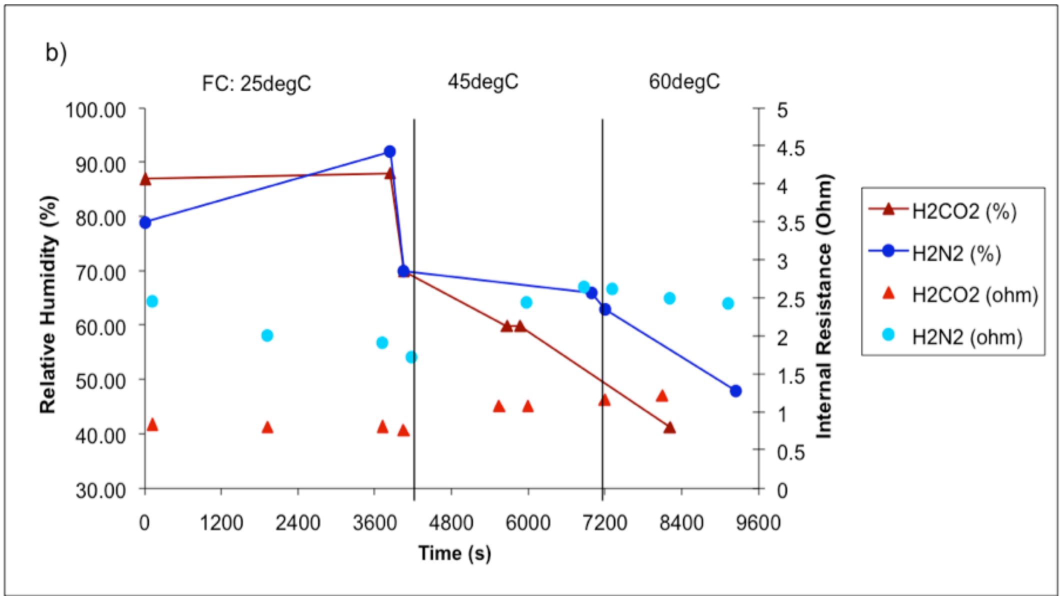

Figure 17. Effect of temperature change on $60H_2/15CO_2$ and $60H_2/15N_2$ hydrogen pumping. The graph details changes in voltage, internal resistance, and relative humidity at fuel cell temperatures of 25, 45, and 60°C. The humidifier tank was set to a constant 55°C. a) The open circuit voltage readings counteracted Figure 16's results by yielding the expected trend of a voltage decrease at all fuel cell temperatures over time. b) The pulsed internal resistance and relative humidity data reflected that a faster drying out of the MEA and feeds at high fuel cell temperatures counteracted competitive hydrogen adsorption.

The decrease in voltage at all fuel cell temperatures and the increase in internal resistance through time erased the peculiarity of open circuit voltage seen in Figure 16a. The decreasing voltage was expected under hydrogen pumping since there was no O_2 to react with incoming H_2 to produce water. As addressed from Figure 16, the highest internal resistances were achieved with fuel cell at 55°C regardless of the tank's temperature, indicating that the humidified gas stream was drying out quickly before reaching the MEA.

Although Figure 17 addressed the peculiarity of Figure 16a, it introduced a new one: the H_2/CO_2 run produced higher voltage than the H_2/N_2 run. CO_2 adsorbs and poisons the Pt catalyst while N_2, an inert gas, does not competitive adsorb with H_2. Since CO_2 undergoes competitive adsorption with reactant H_2, the H_2/CO_2 run should yield at least an order of magnitude lower voltage than did the H_2/N_2 run. Prior to undergoing hydrogen pumping, the fuel cell was operated at dry H_2/O_2 feeds under standard hydrogen fuel cell operation at room temperature for >2hrs to humidify and flush out CO_2 from the catalyst. The high voltage seen on the H_2/CO_2 runs might be caused by a potential difference resulting from the residual O_2 of the previous H_2/O_2 run. Given standard hydrogen fuel cell operation with H_2/O_2 prior to the runs, the high internal resistance of the H_2/N_2 run is hard to explain. Both CO_2 and N_2 inlet streams should yield the same relative humidity at the same flow rates and temperatures. The discrepancy shown in Figure 17b should disappear when the tests are repeated.

iii. H_2/CO_2 Current Sweep

The humidity tests indicated that regardless of fuel cell temperatures, H_2/CO_2 runs with tank temperature of 55°C yielded the highest voltage. At this tank temperature, H_2/CO_2 current sweep to 0.53A was performed at fuel cell temperatures 25, 45, and 60°C. Figure 18 indicates current sweep results to determine the fuel cell temperature allowing for most hydrogen pumping (reflected on graph as runs with highest voltage at highest currents). In-between the current sweeps, open circuit voltage was recorded. The hydrogen pumping operation was conducted with $60H_2/15CO_2$ to stay consistent with previous runs.

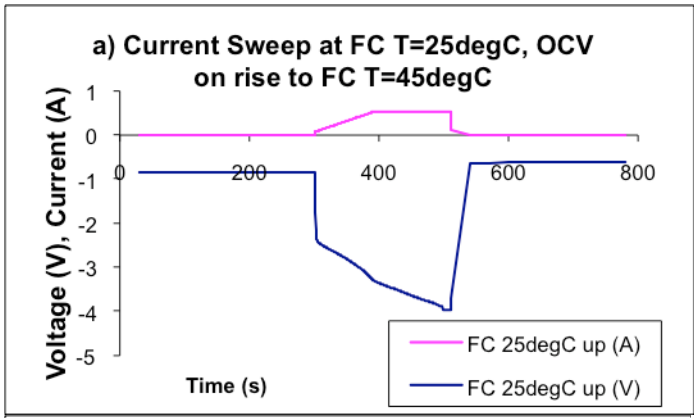
a) Current Sweep at FC T=25degC, OCV on rise to FC T=45degC
Voltage (V), Current (A)
1
0
-1
-2
-3
-4
-5
0
200
400
600
800
Time (s)
FC 25degC up (A)
FC 25degC up (V)

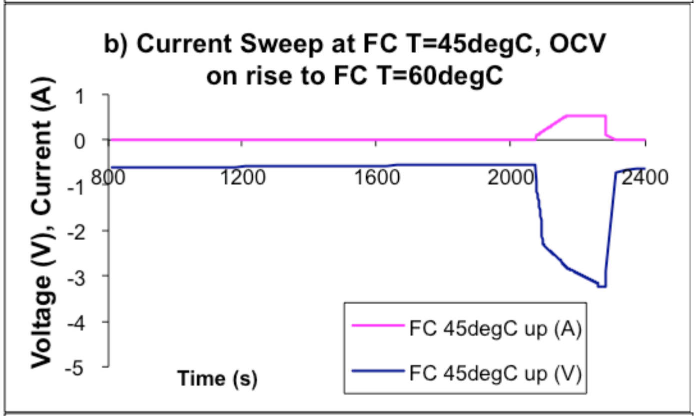
b) Current Sweep at FC T=45degC, OCV on rise to FC T=60degC
Voltage (V), Current (A)
1
0
-1
-2
-3
-4
-5
800
1200
1600
2000
2400
Time (s)
FC 45degC up (A)
FC 45degC up (V)

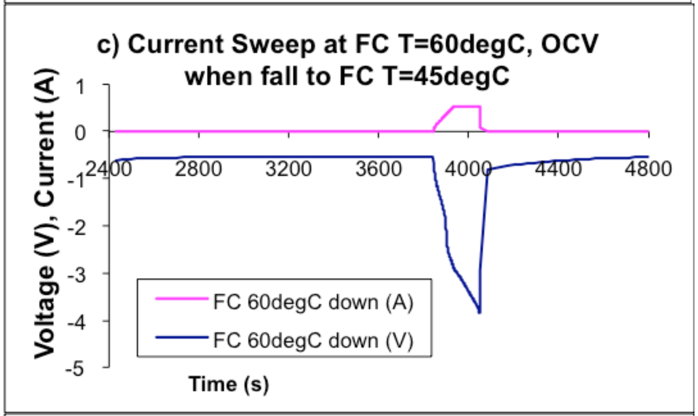
c) Current Sweep at FC T=60degC, OCV when fall to FC T=45degC
Voltage (V), Current (A)
1
0
-1
-2
-3
-4
-5
2400
2800
3200
3600
4000
4400
4800
Time (s)
FC 60degC down (A)
FC 60degC down (V)

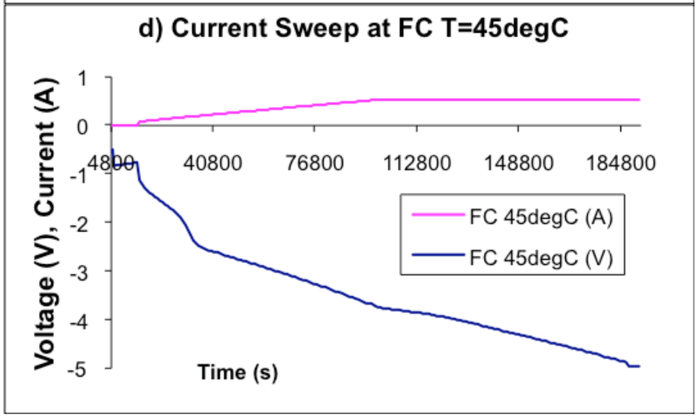
d) Current Sweep at FC T=45degC
Voltage (V), Current (A)
1
0
-1
-2
-3
-4
-5
4800
40800
76800
112800
148800
184800
Time (s)
FC 45degC (A)
FC 45degC (V)

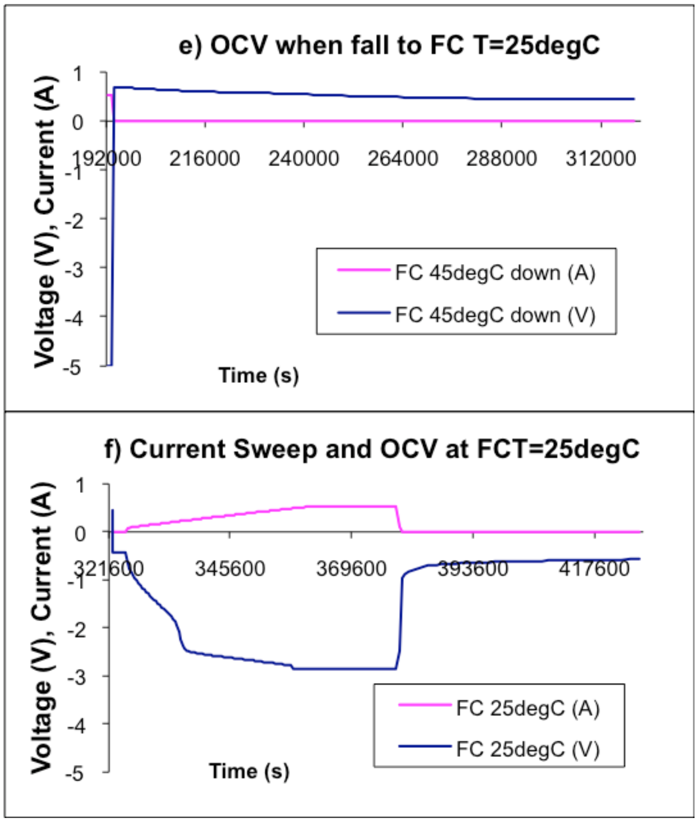

Figure 18. CS and OCV for 60H_2/15CO_2 hydrogen pumping. The results show voltage and current fluctuations as the fuel cell's temperature increased from 25 to 65^{o}C and decreased back down to 25^{o}C. The humidifier tank was set to a constant 55^{o}C.

Although the humidity tests indicated increased internal resistance and decreased relative humidity at fuel cell of 60^{o}C, the runs in Figure 18 still included this fuel cell temperature to address sensitivity of temperature increases on catalyst poisoning. Since the fuel cell's cartridge heaters were more powerful than the heater to the humidifier tank, an approach to slowdown membrane drying before humidified feed arrival was to give the cartridge heaters gradually higher set points until 60^{o}C was reached. Current sweep was set to 0.53A in order to ensure all runs (except the run at graph d) could complete before Arbin's safety voltage limit terminated the schedules. Current increased at a rate of 0.005A/s.

Open circuit voltage showed no sensitivity to temperature changes in-between current sweeps. Unlike the humidity tests, the H_2/CO_2 runs indicated that increased fuel cell temperatures facilitated hydrogen pumping since higher voltage was reached at higher currents (graphs b and c). In contrast, decreased fuel cell temperatures hindered hydrogen pumping (graph d). An explanation is that at higher fuel cell temperatures, the MEA was more active (either from more competitive H_2 adsorption on the catalyst or more water membrane activity due to the preservation of humidity of the feeds) to facilitate hydrogen pumping. Graphs a, b, c and f indicate the potential to pump more hydrogen beyond 0.53A. Graphs a and f reflected the previous view that the lowest fuel cell temperature of 25^{o}C dried the MEA the least so hydrogen pumping is facilitated. The overall voltage decreases as more current is supplied (Equation 4).

Since increased fuel cell temperatures indicated the potential for hydrogen pumping beyond 0.53A, a new run was analyzed with the humidifier tank at 55^{o}C and fuel cell at 60^{o}C. Figure 19 indicated the hydrogen pumping result at current increase of 0.005A/s to 1.08A for $60H_2/15CO_2$ and $60H_2/15N_2$ feeds. Given the same temperatures and water quantity in the humidifier tank, the fact that the H_2/CO_2 run pumped more hydrogen than the H_2/N_2 run indicated that higher fuel cell temperatures made H_2 adsorption more competitive.

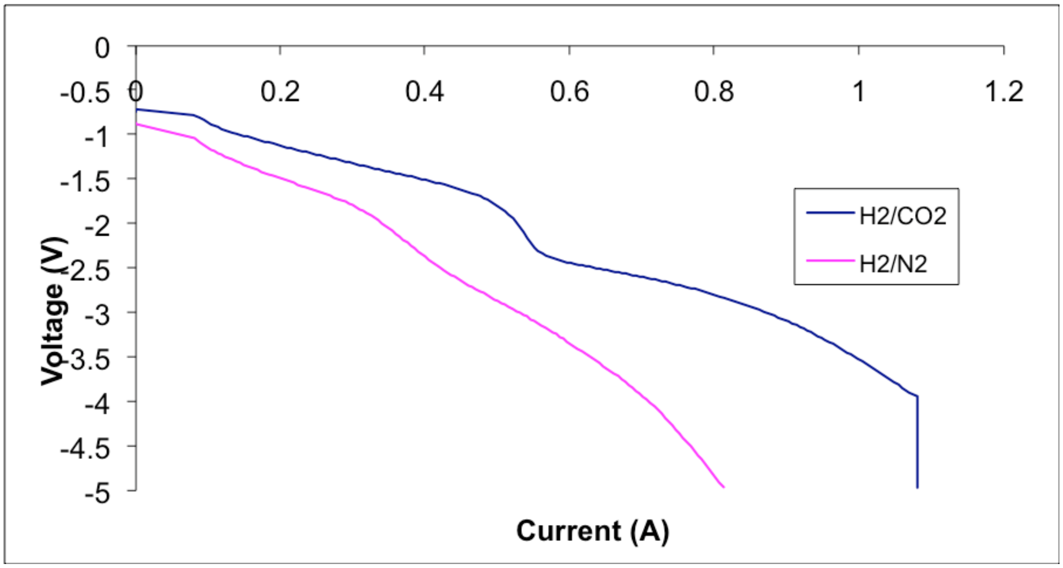

Figure 19. Current sweep for $60H_2/15CO_2$ and $60H_2/15N_2$ inlet gas streams. The $60H_2/15N_2$ could not reach the desired 1.08A current sweep. The $60H_2/15CO_2$ reached but could not sustain at 1.08A before Arbin terminated the schedule.

During hydrogen pumping, gas bubbles emerged from the cathode outlet around 0.4A. According to Equation 10 (rearranged to determine Q), given the fuel cell temperature of 60^oC at 0.4A, the cathode outlet gas flow rate is 3.40mL/s. Since the gas bubbles had to travel along the cathode tube before reaching the outlet, it implied that gas bubbles must have formed earlier, probably around 0.2A, which gives flow rate 1.67mL/min.

Arbin's safety voltage limit precluded the H_2/CO_2 run from sustaining current at 1.08A, and terminated the H_2/N_2 run before reaching 1.08A. If the first few gas bubbles out of the cathode outlet were diffused N_2 or CO_2, pure H_2 could be collected past the N_2 and CO_2 diffusion times (since at 75mL feed, $\tau_D > \tau_R$).

iv. High-Slope Voltage Region

In current sweep runs employing H_2/O_2, H_2/N_2, and H_2/CO_2, the IV curves had a high-slope voltage region (Figures 13, 15, and 19). The region disappeared when the cathode inlet was not sealed. Figure 20 shows $60H_2/15N_2$ current sweeps at 0.005A/s at tank temperature 55°C and fuel cell temperature 60°C. The green data set indicates the run with an uncapped cathode inlet. The more gradual slope in voltage in the uncapped data set suggested that the fuel cell was able to extract oxygen from the air at the cathode inlet. Since the presence of oxygen in the uncapped test does not explain the high-slope voltage region in capped tests, other tests were run.

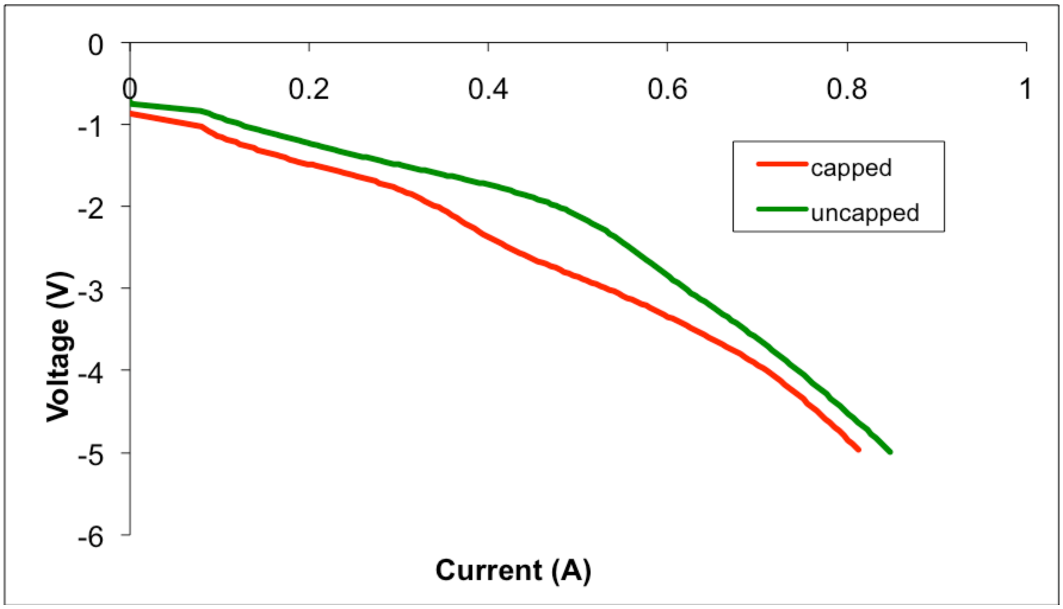

Figure 20. Capped and uncapped runs at $60H_2/15N_2$, current sweep rate of 0.005A/s, tank at 55°C and fuel cell at 60°C. The uncapped run showed a more gradual slope in voltage, due to the presence of oxygen.

Figure 21 shows runs for current control at tank 55°C, $60H_2/15CO_2$ feeds, and varying fuel cell temperatures (25, 45, 60°C) to analyze the high-slope voltage region. Voltage was recorded at times when the fuel cell stayed at rest, 0.00A, 0.25A, and 0.70A.

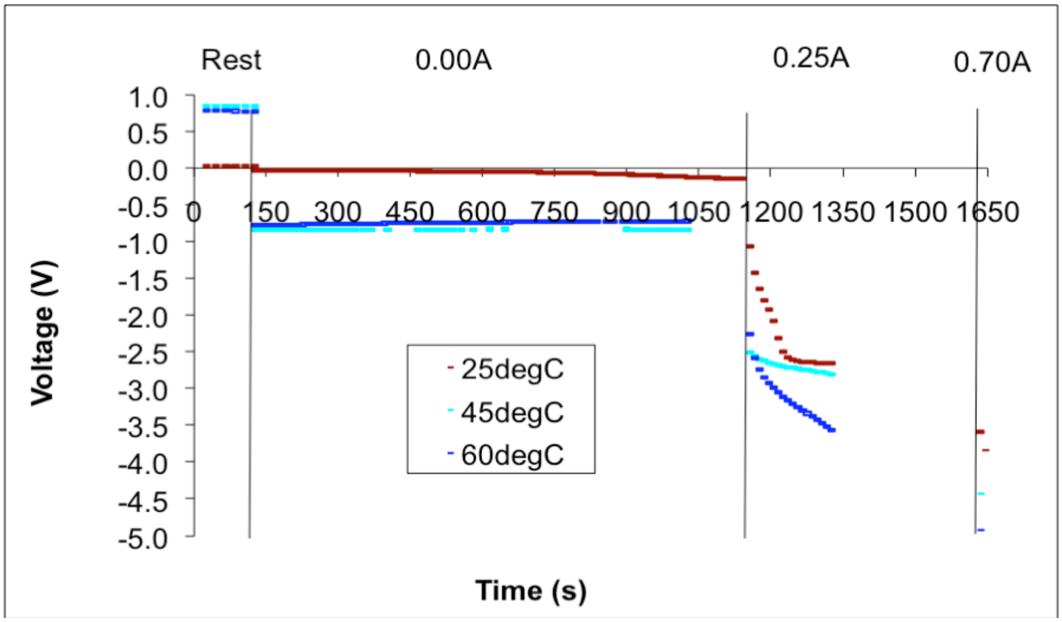

Figure 21. Investigating high-slope voltage region via current control. Current control involved rest, 0.00A, 0.25A, and 0.70A on $60H_2/15CO_2$ inlet gas streams and tank 55°C. Individual high-slope voltage regions were observed at 0.25A and 0.70A.

Current control at 0.25A and 0.70A recorded fewer data points. If their individual high-slope voltage regions were to be maintained, Arbin's safety voltage limit would have terminated the schedules. The voltages at rest and at 0.00A current control had different signs. At rest, the difference in hydrogen partial pressures at the electrodes led Arbin to record positive voltage based on Equation 6. At 0.00A current control, Arbin supplied its own current in order to detect a current reading, which according to Equation 4 led to a negative voltage reading. At 0.25A, fuel cells at all temperatures exhibited high-slope voltage regions prior to leveling off to steady voltage. At 0.70A, Arbin's safety voltage limit disabled the collection of more data points but a high-slope voltage region was expected.

The high-slope voltage limit occurring as low as 0.25A might indicate an initial mass transfer limit that disappeared as H_2 supplied more protons and electrons at the anode. The eventual leveling off to constant voltage indicated the shift away from mass transfer limit to reaction equilibrium. Presumably, a similar high-slope voltage region would be detected at 0.70A, given excess H_2 reactant. The same explanation might apply to Figure 19's high-slope voltage region, where the high-slope voltage region at 0.4-0.6A is a self-inflicted mass transfer limit that disappeared after reactant H_2 had time to buildup and equilibrate at the anode. The final high-slope voltage region starting after 0.8A indicated the natural mass transfer limit based on intrinsic gas properties. This explanation addresses the insensitivity of the initial high-slope voltage region to applied current (since it occurs around 0.2A (Figures 15 and 21) and around 0.4-0.6A (Figures 14, 19, and 20)). It also addresses the sensitivity of the final high-slope voltage region to different gas feeds (since the natural mass transfer limit is based on intrinsic gas properties). If the current sweep rate is <0.005A/s, the initial high-slope voltage region should disappear, leaving only the natural mass transfer limit.

To avoid Arbin's safety voltage limit, hydrogen pumping was conducted manually at tank of $55^{o}C$, fuel cell of $45^{o}C$, and $80H_2/20CO_2$ feeds. The tank temperature was chosen since Figure 19 indicated a positive effect of fuel cell temperature on H_2 competitive adsorption. The fuel cell temperature of $45^{o}C$ was chosen since Figure 18's graph b indicated its potential for more hydrogen pumping. The $80H_2/20CO_2$ feed was used to preserve the 4:1 H_2/CO_2 ratio of past runs.

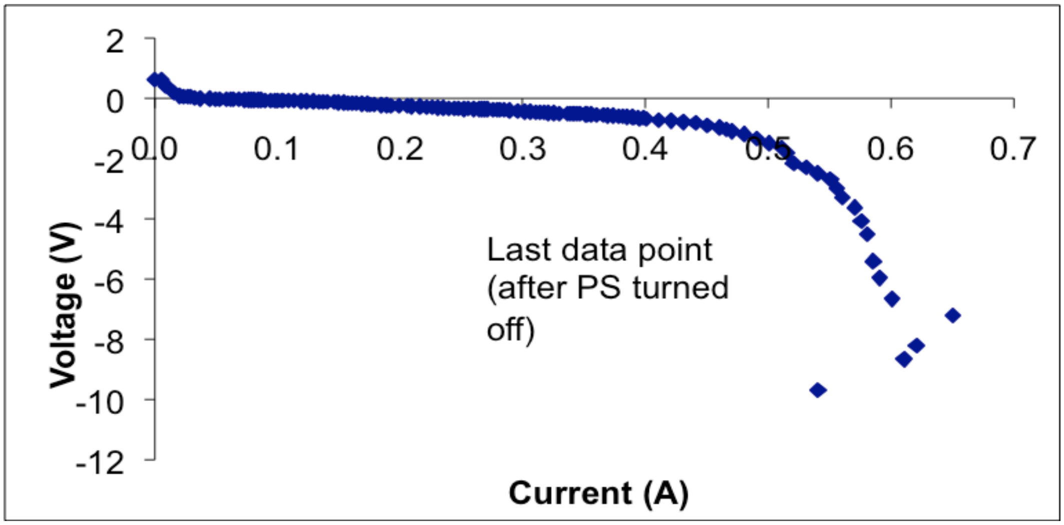

Figure 22. Manual current sweep with $80H_2/20CO_2$ inlet gas stream under hydrogen pumping. The humidifier tank was set at 55°C; fuel cell at 45°C. At current sweep <0.005A/s, the initial high-slope voltage region found on earlier runs was eliminated.

The manual run conducted at 0.005A/s eliminated the initial high-slope voltage region found on earlier runs, keeping only the final high-slope voltage region (Figure 22). The result seemed consistent with the explanation that the initial high-slope voltage region was a self-inflicted mass transfer limit that would be eliminated at slower than 0.005A/s current sweep rate. The initial positive voltage is likely caused by residual O_2 from the overnite H_2/O_2 run prior to conducting the experiment. At the activation region ($i<0.2A/cm^2$), the sharp decrease in voltage is attributed to the barrier for electron transfer reactions at the electrodes. The HP 6114A Precision Power Supply applied at most 10V for hydrogen pumping to 0.61A and the flow rates for the pumped hydrogen was recorded via bubblemeter every 15min. The outlet gas flow rates recorded for the three 15min sections were 0.00095, 0.00037, and 0.00026mL/min. The decrease in flow rate resulted from the shutdown of the power supply past 10V.

The flow rate in the cathode outlet gas stream is calculated for various temperatures and current based on Equation 10 (Figure 23). All of the experimental flow rates were lower than that calculated. The lower experimental values occur most likely as a result of reactant hydrogen crossover from the anode to the cathode.

Figure 23. Table of flow rates showing theoretical and actual gas flow rates at the cathode outlet used throughout the current sweeps in this study.

	H2 Flowrate at Cathode Outlet					
	Flowrate Q =	nRT/P	Parameters			
			R (J/molK)	8.314		
			P (J/m3)	1.013E+05		
			F (C/mol)	96485	*Theoretical*	*Actual*
Experiment	**Temperature**	**degC**	**K**	**A**	**mL/min**	**mL/min**
H2/N2, no tank	FC Temp.	25	298	1.00	7.60	6.9
H2/CO2, tank	FC Temp.	25	298	0.53	4.03	1.83
H2/CO2, tank	FC Temp.	60	333	0.53	4.50	1.79
H2/CO2, tank	Hum Temp.	55	328	0.61	5.11	0.00095
H2/CO2, tank	FC Temp.	45	318	0.61	4.95	0.00095

5. Conclusions and Future Work

A STR PEM fuel cell under standard stoichiometric H_2/O_2 fuel cell feeds underwent potentiostatic operation to detect internal resistance. Despite variations in the membrane water activity on different days, the power performance curves yielded the same order of magnitude of internal resistance $\leq 1.58\Omega$. Low internal resistance reflected good three-phase interface between electrolyte, catalyst, and reactant gas, and sufficient membrane water activity, paving the way for more runs with the same fuel cell and MEA. IV curves were then generated from galvanostatic operation of various feeds via a HP 6114A Precision Power Supply. The Arbin Instruments MSTAT4+ software successfully reproduced the manual galvanostatic tests and became the default instrument for hydrogen pumping.

Fuel cell feeds for hydrogen pumping were passed through a humidifier tank to prevent the membrane from drying out in the absence of O_2. Humidity tests were conducted to find the proper settings for hydrogen pumping. When both the tank and fuel cell temperatures were adjusted, the combination of $60H_2/15CO_2$ runs yielding the highest open circuit voltage and the lowest internal resistance was fuel cell at 25^oC and tank at 55^oC. The fact that higher fuel cell temperatures neither maintained humidity of the inlet streams nor improved fuel cell voltage via decreased CO_2 poisoning was unexpected. An explanation is that fuel cells at higher temperatures counteracted the effect of the humidifier tank by drying out the humidified feeds, thereby increasing internal resistance.

The humidity tests indicated that regardless of fuel cell temperatures, H_2/CO_2 runs with tank temperature of 55°C yielded the highest voltage. The H_2/CO_2 runs indicated that increased fuel cell temperatures facilitated hydrogen pumping since higher voltage was reached at higher currents. In contrast, decreased fuel cell temperatures hindered hydrogen pumping. Since increased fuel cell temperatures indicated the potential for hydrogen pumping, hydrogen pumping runs comparing H_2/CO_2 and H_2/N_2 indicated that higher fuel cell temperatures made H_2 adsorption more competitive.

During hydrogen pumping, gas bubbles emerged from the cathode outlet and were calculated based on Equation 10. Arbin's safety voltage limit precluded hydrogen pumping runs from sustaining current. If current can be sustained, assuming the first few gas bubbles out of the cathode outlet were diffused N_2 or CO_2, pure H_2 could be collected past the N_2 and CO_2 diffusion times.

In current sweep runs employing H_2/O_2, H_2/N_2, and H_2/CO_2, the IV curves had a high-slope voltage region. Runs for current control at tank 55°C, $60H_2/15CO_2$ feeds, and varying fuel cell temperatures (25, 45, 60°C) were conducted to analyze the high-slope voltage region. Manual hydrogen pumping to avoid Arbin's safety voltage limit were conducted as well. The manual run seems to indicate that the initial high-slope voltage region is a self-inflicted mass transfer limit that would be eliminated at slower than 0.005A/s current sweep rate.

This study assumed the fuel cell to operate as a STR. Future work should consider the fuel cell as a plug flow reactor (PFR), which would allow larger reductions of hydrogen partial pressures between the anode and cathode to facilitate hydrogen pumping.

The experimental setup can be improved with equal-powered heaters with temperature control at the tank and fuel cell, and insulated tubing extending from the tank outlet to the fuel cell inlet. This will prevent drying out of the humidified inlet stream and MEA.

The Arbin program has a safety mechanism that shuts off schedules when the voltage reaches beyond $|\pm 5\text{V}|$. This mechanism prevented the fuel cell from maintaining the desired current long enough to collect a steady gas stream from the cathode outlet. The problem could be circumvented in future work in four ways: change Arbin's safety voltage limit to a greater magnitude, employ commercial MEA using Nafion 112 to increase the fuel cell's current density (to prevent overall voltage from reaching Arbin's limit), optimize the relative humidity of the inlet stream to prevent drying out of the MEA, or forgo the automated Arbin setup for the galvanostatic manual setup.

6. Appendix

a. Fuel Cell Blueprint

The blueprint of the STR PEM fuel cell shows the block composition, 1/8” deep inlet flow channels at the electrodes, diamond-shaped graphite open gas plenums supported by four pillars, active fuel cell area (~$1.9 cm^2$), and 45^oC tilt of outlets.

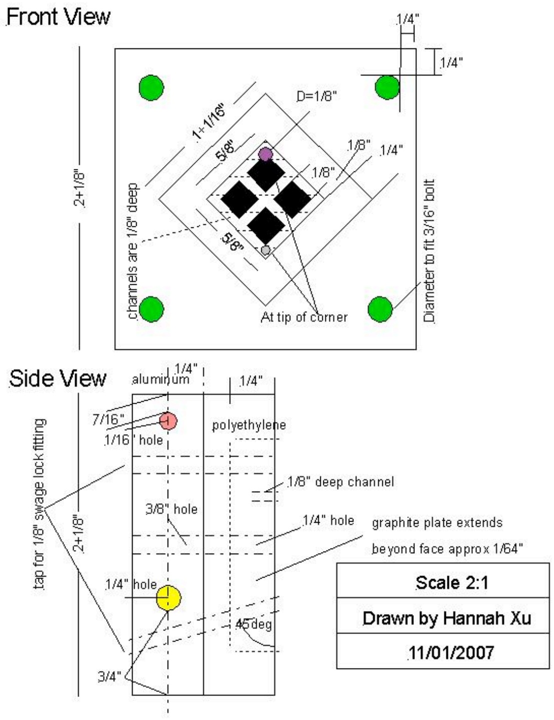

b. Arbin Schedules

After Arbin’s green and black connectors were attached to the fuel cell’s anode and the red and white connectors were attached to the fuel cell’s cathode, Arbin monitored the voltage, current, and internal resistance of the fuel cell following Current Sweep and/or Open Circuit Voltage schedules.

i. Current Sweep

The Current Sweep schedule pumped hydrogen from the anode to the cathode of the fuel cell by sweeping current at a certain rate. Internal resistance was determined in pulses. In this sample schedule, the rate of current sweep is 0.002A/s while the internal resistance is checked 2 minutes after the schedule begins and 2 minutes before the schedule ends.

		Step Label	Number Of Limits	Control Type	Control Value	Extra Control Value 1	Extra Control Value 2	Current Range
1	☒	Step_A	2	Rest				
		Log Limit	**Step Limit**	**Goto Step**	**Type1**	**Sign1**	**Value1**	**Type2**
	1	☒	☒	Next Step	PV_CHAN_Step_Time	>=	00:02:00	
	2	☒	☐		DV_Time	>=	00:00:05	
2	☒	Step_B	1	Internal Resistance	Amp:0.04	ms:1.00	Offset:0	Low
		Log Limit	**Step Limit**	**Goto Step**	**Type1**	**Sign1**	**Value1**	**Type2**
	1	☒	☒	Next Step	PV_CHAN_Step_Time	>=	00:00:00	
3	☒	Step_C1	2	Current Ramp(A)	Start:0	dI/sec:0.001		Medium
		Log Limit	**Step Limit**	**Goto Step**	**Type1**	**Sign1**	**Value1**	**Type2**
	1	☒	☒	Next Step	PV_CHAN_Step_Time	>=	00:01:40	
	2	☒	☐		DV_Time	>=	00:00:01	
4	☒	Step_D1	2	Current Ramp(A)	Start:0.1	dI/sec:0.002		High
		Log Limit	**Step Limit**	**Goto Step**	**Type1**	**Sign1**	**Value1**	**Type2**
	1	☒	☒	Next Step	PV_CHAN_Step_Time	>=	00:07:30	
	2	☒	☐		DV_Time	>=	00:00:01	
5	☒	Step_H	2	Current(A)	1			High
		Log Limit	**Step Limit**	**Goto Step**	**Type1**	**Sign1**	**Value1**	**Type2**
	1	☒	☒	Next Step	PV_CHAN_Step_Time	>=	00:05:00	
	2	☒	☐		DV_Time	>=	00:00:15	
6	☒	Step_K	1	Internal Resistance	Amp:0.04	ms:1.00	Offset:0	Low
		Log Limit	**Step Limit**	**Goto Step**	**Type1**	**Sign1**	**Value1**	**Type2**
	1	☒	☒	Next Step	PV_CHAN_Step_Time	>=	00:00:00	
7	☒	Step_J	2	Rest				
		Log Limit	**Step Limit**	**Goto Step**	**Type1**	**Sign1**	**Value1**	**Type2**
	1	☒	☒	Next Step	PV_CHAN_Step_Time	>=	00:02:00	
	2	☒	☐		DV_Time	>=	00:00:10	
8	☒	Step_F	2	Rest				
		Log Limit	**Step Limit**	**Goto Step**	**Type1**	**Sign1**	**Value1**	**Type2**
	1	☒	☒	Next Step	PV_CHAN_Step_Time	>=	00:00:00	
	2	☒	☒	End Test	PV_CHAN_Step_Time	>=	00:00:00	

ii. Open Circuit Voltage

The Rest step determines the fuel cell’s open circuit voltage (OCV). There is no current control. This sample schedule indicates that voltage is recorded every 10 seconds and the internal resistance is checked every 15 minutes.

		Step Label	Number Of Limits	Control Type	Control Value	Extra Control Value 1	Extra Control Value 2	Current Range
1	✖	Step_A	2	Rest				
		Log Limit	**Step Limit**	**Goto Step**	**Type1**	**Sign1**	**Value1**	**Type2**
	1	☒	☒	Next Step	PV_CHAN_Step_Time	>=	00:02:00	
	2	☒	☐		DV_Time	>=	00:00:10	
2	✖	Step_B	1	Internal Resistance	Amp:0.04	ms:1.00	Offset:0	Low
		Log Limit	**Step Limit**	**Goto Step**	**Type1**	**Sign1**	**Value1**	**Type2**
	1	☒	☒	Next Step	PV_CHAN_Step_Time	>=	00:00:00	
3	✖	Step_C	2	Rest				
		Log Limit	**Step Limit**	**Goto Step**	**Type1**	**Sign1**	**Value1**	**Type2**
	1	☒	☒	Next Step	PV_CHAN_Step_Time	>=	00:15:00	
	2	☒	☐		DV_Time	>=	00:00:30	
4	✖	Step_D	1	Internal Resistance	Amp:0.04	ms:1.00	Offset:0	High
		Log Limit	**Step Limit**	**Goto Step**	**Type1**	**Sign1**	**Value1**	**Type2**
	1	☒	☒	Next Step	PV_CHAN_Step_Time	>=	00:00:00	
5	✖	Step_E	2	Rest				
		Log Limit	**Step Limit**	**Goto Step**	**Type1**	**Sign1**	**Value1**	**Type2**
	1	☒	☒	Next Step	PV_CHAN_Step_Time	>=	00:15:00	
	2	☒	☐		DV_Time	>=	00:00:30	
6	✖	Step_F	1	Internal Resistance	Amp:0.04	ms:1.00	Offset:0	Low
		Log Limit	**Step Limit**	**Goto Step**	**Type1**	**Sign1**	**Value1**	**Type2**
	1	☒	☒	Next Step	PV_CHAN_Step_Time	>=	00:00:00	
7	✖	Step_G	2	Rest				
		Log Limit	**Step Limit**	**Goto Step**	**Type1**	**Sign1**	**Value1**	**Type2**
	1	☒	☒	Next Step	PV_CHAN_Step_Time	>=	00:02:00	
	2	☒	☐		DV_Time	>=	00:00:10	
8	✖	Step_H	2	Rest				
		Log Limit	**Step Limit**	**Goto Step**	**Type1**	**Sign1**	**Value1**	**Type2**
	1	☒	☒	Next Step	PV_CHAN_Step_Time	>=	00:00:00	
	2	☒	☒	End Test	PV_CHAN_Step_Time	>=	00:00:00	

7. References

1. Adhikari, S. and S. Fernando. “Hydrogen Membrane Separation Techniques.” *Industrial and Engineering Chemistry Research*, **45**, 2006, 875-881.

2. Baschuk, J.J., and X.H.Li, Modeling of Polymer Electrolyte Membraen Fuel cells with Variable Degrees of Water Flooding, *J. Power Sources*, **86**, 181 (2000).

3. Benziger, J., et. al.“Stirred Tank Reactor Polymer Electrolyte Membrane Fuel cell.” AIChE J., 50, 1889, 2004.

4. Benziger, J., et. al. “Water Balance and Multiplicity in a Polymer Electrolyte Membrane Fuel cell.” AIChE J., 50, 2320.

5. Benziger, J., et. al. “Steady State Multiplicity in a Polymer Electrolyte Membrane Fuel cell.” AIChE J., 509, 2320, 2004.

6. Benziger, J., et. al. “Steady State Multiplicity in the Autohumidification Polymer Electrolyte Membrane Fuel cell.” Chem. Eng. Sci., 58, 4705, 2003.

7. Benziger, J., et. al. “Silicon Oxide Nafion Composite Membranes for Proton-Exchange Membrane Fuel cell Operation at 80-140 degrees C.” J. Electrochem. Soc., 149, A256, 2002.

8. Benziger, J., et. al. “Investigation of PEMFUEL CELL Operation Above 100 degrees C Employing Perfluorosulfonic Acid Silicon Oxide Composite Membranes.” J. Power Sources, 109, 356, 2002.

9. Benziger, J. “Reactor Dynamics of PEM Fuel cells.” Internal.

10. Benziger, J. and W. Hogarth. “Dynamics of Autohumidified PEM Fuel cell Operation.” J. Electrochem. Soc., 153, A2139, 2006.

11. Benziger et al. Power Performance Curve for Engineering Analysis of Fuel cells, *Journal of Power Sources*, **155**, 2006, 272-285.

12. Blomen, L.J.M.J., and M.N.Mugerwa, eds., *Fuel Cell Systems*, Plenum, New York (1993).

13. Bokris, J.O.M., and S. Srinivasan, *Fuel Cells: Their Electrochemistry*, McGraw-Hill, New York (1969).

14. Buchi, F.N., and Srinivasan, S. (1997). Operating proton exchange membrane fuel cells without external humidification of the reactant gases- fundamental aspects. *Journal of the Electrochemical Society*, **144**(8), 2767-2772.

15. Corradetti, A., and U. Desideri. (2007). A technoeconomic analysis of different options for cogenerating power in hydrogen plants based on natural

gas reforming. *Journal of Engineering for Gas Turbines and Power*, **129**, 338-351.

16. EG&G Services, *Fuel cell Handbook*, 5th Edition. Parsons Inc. October 2000.
17. Gottesfeld, S., and T. Zawodinski, Polymer electrolyte fuel cells, *Advances in Electrochemical Science and Engineering*. **5** (1997) 195-301.
18. Jian Z., and W.S. Winston Ho. (2007). Hydrogen purification for fuel cells by carbon dioxide removal membrane followed by water gas shift reaction. *Journal of Chemical Engineering of Japan*, **40** (11), 1011-1020.
19. Karnas, E. "STR PEM Fuel cells: Response to Changes in System Parameters." Internal (REU Summer 2003).
20. Kluiters, S. C. A. *Status review on membrane systems for hydrogen separation*; Energy Center of the Netherlands: Petten, the Netherlands, 2004.
21. Lee et al. Remarkable Improvement in Hydrogen Recovery and Reaction Efficiency of a Methanol Reforming- Membrane Reactor by Using a Novel Knudsen Membrane, *Industrial and Engineering Chemistry Research*, **47**, 2008, 1392-1397.
22. Moxley, J.F., Tulyani S. and J. Benziger. Steady-state multiplicity in the autohumidification polymer electrolyte membrane fuel cell. *Chemical Engineering Science* **58** (2003), 4705-4708.
23. Ogden, J.M. *Prospects for building a hydrogen energy infrastructure*; Center for Energy and Environmental Studies, Princeton University: Princeton, NJ, 1999.
24. Parson, I. EG&G Services. *Fuel Cell Handbook*. U.S. Department of Energy, Morgantown, WV, 2000.
25. Perry, K., Eisman, G., and B. Benicewicz. (2007). Electrochemical hydrogen pumping using a high-temperature polybenzimidazole (PBI) membrane. *Journal of Power Sources*, **177**, 478-484.
26. Pukrushpan, J.; Stefanopoulou A.G.; and Peng H. Control of Fuel cell Breathing, *IEEE Control Systems Magazine*, 20004, 30-46.
27. Rosen, M.A.; Scott, D. S. Comparative efficiency assessment for a range of hydrogen production processes. *Int. J.* Hydrogen Energy 1998, 23, 631-640.
28. Sircar, S.; Golden, T. C. Purification of hydrogen by pressure swing adsorption. *Sep. Sci. Technol*. **2000**, 35, 667-687.
29. Srinivasan, S., et al., in: L.J.M.J. in Fuel Cell Systems, M.N. Blomen, Mugerwa (Eds.), *Overview of Fuel Cell Technology*, Plenum Press, New York, 1993, pp. 37-72.

30. Stocker, J.; Whysall, M.; Miller, G.Q. *30 years of PSA technology for hydrogen purification 2005;* UOP LLC: Des Planies, IL, 1998.

31. Thampan, T., Malhotra, S., Tang, H., and Datta, R. (2000). Modeling of conductive transport in proton-exchange membranes for fuel cells. *Journal of the Electrochemical Society*, **147**(9), 3242-3250.

32. Uppal, A., Ray, W.H., and Pore, A. B. (1974). Dynamic behavior of continuous stirred tank reactors. *Chemical Engineering Science*, **29**(4), 967-985.

33. Watanabe, M., Uchida, H., Seki, Y., Emori, M., Sonehart, P. (1996). Self-humidifying polymer electrolyte membranes for fuel cells. *Journal of the Electrochemical Society*, **143**(12), 3847-3852.

34. Weber, A.Z., and J. Newman. Modeling transport in polymer-electrolyte fuel cells, Chem. Rev. 104 (10) (2004) 4679-4726.

35. Yang, C., Costamagna, P., Srinivasan, S., Benziger, J., and A.B. Bocarsly. (2001). Approaches and technical challenges to high temperature operation of proton exchange membrane fuel cells. *Journal of Power Sources*, **103**(1), 1-9.